Interplay between tidal flows and magnetic fields in non-linear simulations of stellar and planetary convective envelopes

Aurélie Astoul ⬤⋆ and Adrian J. Barker ⬤⋆

School of Mathematics, University of Leeds, Leeds LS2 9JT, UK

ABSTRACT

Stars and planets in close systems are magnetized, but the influence of magnetic fields on their tidal responses (and vice versa) and dissipation rates has not been well explored. We present exploratory non-linear magnetohydrodynamical (MHD) simulations of tidally excited inertial waves in convective envelopes. These waves probably provide the dominant contribution to tidal dissipation in several astrophysical settings, including tidal circularization of solar-type binary stars and hot Jupiters, and orbital migration of the moons of Jupiter and Saturn. We model convective envelopes as incompressible magnetized fluids in spherical shells harbouring an initially (rotationally aligned) dipolar magnetic field. We find that depending on its strength (quantified by its Lehnert number Le) and the magnetic Prandtl number Pm, the magnetic field can either deeply modify the tidal response or be substantially altered by tidal flows. Simulations with small Le exhibit strong tidally generated differential rotation (zonal flows) for sufficiently large tidal amplitudes, such that both the amplitude and topology of the initial magnetic field are tidally impacted. In contrast, strong magnetic fields can inhibit these zonal flows through large-scale magnetic torques, and by Maxwell stresses arising from magnetorotational instability, which we identify and characterize in our simulations, along with the role of torsional Alfvén waves. Without tidally driven zonal flows, the resulting tidal dissipation is close to the linear predictions. We quantify the transition Le as a function of Pm, finding it to be comparable to realistic values found in solar-like stars, such that we predict complex interactions between tidal flows and magnetic fields.

Key words: MHD – waves – instabilities – planets and satellites: gaseous planets – planet–star interactions – stars: low-mass – stars: magnetic field.

1 INTRODUCTION

Tidal interactions are a key driver of orbital and rotational evolution in compact stellar and exoplanetary systems (e.g. Ogilvie 2014; Mathis 2019). Solar-like (low-mass) stars and giant gaseous planets feature convective envelopes in which inertial waves restored by Coriolis forces – and in magnetized stars, magneto-inertial waves restored by both Coriolis and Lorentz forces – can be tidally excited. Their dissipation is believed to contribute significantly to angular momentum exchanges and spin–orbit evolution in these systems. For example, simplified calculations indicate that these waves may largely explain the observed orbital evolution of Jupiter's and Saturn's moons (e.g. Ogilvie & Lin 2004; Dewberry 2023; Lin 2023; Dhouib et al. 2024; Pontin, Barker & Hollerbach 2024), the circularization periods of solar-type binary stars (e.g. Barker 2022), and the eccentricity distributions of hot and warm Jupiters (e.g. Lazovik et al. 2024). However, many aspects of these waves in realistic astrophysical environments, like in differentially rotating and/or magnetized envelopes with convective motions and density stratification, and their resulting contributions to tidal dissipation are still poorly understood.

Inertial waves are thought to be particularly important for tidal evolution in systems with fast rotators, such as young stars or Jupiter-like planets. One reason is that inertial waves are only (linearly) excited for tidal frequencies satisfying $|\omega| \leq 2|\Omega_0|$, where ω is the Doppler-shifted frequency in the frame rotating with the stellar angular velocity Ω_0. This condition is more easily satisfied for faster rotation (larger values of Ω_0). Secondly, the (frequency-averaged) tidal dissipation rate scales approximately with the square of the rotational frequency in linear theory (e.g. Ogilvie 2013), so faster rotating stars or planets tend to be more dissipative than more slowly rotating ones (all else being equal), as been shown in Mathis (2015), Bolmont & Mathis (2016), Gallet et al. (2017), and Barker (2020) using 1D stellar evolution models.

The solar convection zone is known to harbour a predominantly dipolar magnetic field with an overall strength of approximately 20 G at the surface, but this varies substantially across the surface and inside the convective envelope (possibly up to several Tesla for sunspot-forming toroidal flux ropes, Charbonneau 2013, 2014). Convective fluid motions are thought to play a key role in the solar dynamo, even if the extent to which this is the case is debated (e.g. Brun & Browning 2017), as well as the location of the dynamo, either deep down in the convective envelope (and top of the radiative layer Parker 1993), in the bulk (e.g. Strugarek et al. 2017), or in the near-surface shear layers (for instance, Vasil et al. 2024). Observations

⋆ E-mail: a.a.v.astoul@leeds.ac.uk (AA); A.J.Barker@leeds.ac.uk (AJB)

also indicate that magnetic fields are ubiquitous in low-mass stars, as revealed by spectropolarimetry (e.g. Donati & Landstreet 2009; Reiners 2012), which probes the large-scale magnetic fields at their surfaces, and as predicted by 3D MHD simulations of convective dynamos (for a review see Käpylä et al. 2023, and references therein).

While Alfvén waves restored by the Lorentz force are the only low frequency (i.e. ignoring surface gravity and acoustic) waves in a magnetized envelope, in a rotating and magnetized medium, mixed types of wave arise due to the combined action of the Coriolis acceleration and magnetic tension. These include slow and fast magneto-inertial waves (also called magneto-Coriolis or MC waves), which arise depending on whether the two restoring forces cancel each other or sum up in the dispersion relation (Lehnert 1954; Malkus 1967; Finlay 2008, for a review). In the latter case, the wave frequency exceeds the cut-off frequency $2\Omega_0$ of inertial waves, while in the former case, the frequency is lower than the rotation frequency and the waves are often called magnetostrophic waves, for fast rotators. Magneto-inertial waves have been largely studied in the context of the geodynamo, as they are expected in the liquid outer core of the Earth, and they have been studied experimentally, for example via rotating spherical Couette flow in liquid metal or sodium experiments (Schmitt et al. 2008, 2013; Le Bars et al. 2022, for a review), or through numerical simulations (e.g. Schmitt 2010; Aubert 2018). One type of wave that arises in this context is torsional Alfvén waves, which are (cylindrically) radially propagating waves in differentially rotating fluids that are invariant along the rotation axis. They may reflect and form standing modes, the so-called torsional oscillations (e.g. Braginskiy 1970; Schaeffer et al. 2017; Hori, Nilsson & Tobias 2023, for a review).

In stellar envelopes, the effect of a magnetic field has been studied on some specific torsional inertial modes (the r modes, as in Lander, Jones & Passamonti 2010; Abbassi, Rieutord & Rezania 2012, for neutron stars), and the propagation of shear Alfvén waves (with dissipative processes) has been investigated by Rincon & Rieutord (2003) and Reese, Rincon & Rieutord (2004) in incompressible (though non-rotating) shells with a dipolar magnetic field. Very few global non-linear studies have been performed to explore the tidal response and its dissipation in convective envelopes of rotating stars and planets (e.g. Tilgner 2007; Favier et al. 2014; Astoul & Barker 2022, 2023), and none with a magnetic field (though Cébron & Hollerbach 2014, simulated the elliptical instability in a full sphere in the presence of a magnetic field to study tidal dynamos). Previous theoretical studies of tidal inertial waves have primarily involved linear calculations or explored non-linear tidal waves in the absence of magnetic fields. With rotation, an important prior study is Lin & Ogilvie (2018, see also Wei 2016 in a local box), who performed linear calculations of tidal magneto-inertial waves in convective envelopes with an imposed rotationally aligned dipolar magnetic field (or a uniform field aligned with the rotation axis, also in Wei 2018, for rapid rotators). They found that the (low-frequency) frequency-averaged tidal dissipation when inertial waves are excited is unmodified by a magnetic field. However, the dissipation at a given frequency, as well as the nature of the waves and the mechanisms of their dissipation – whether this is due to viscosity or Ohmic diffusion, and whether it is due to turbulent or microscopic processes – can be very different when considering a magnetic field. Considering stellar tides in hot Jupiter systems,[1] it has been shown that magnetic effects

should not be neglected when computing tidal dissipation at a given frequency (Astoul et al. 2019).

This motivates us to study here the interplay between tidal flows and magnetism using 3D non-linear simulations of rotating stellar or planetary convection zones, building upon our prior hydrodynamical studies in Astoul & Barker (2022, hereafter AB22) and Astoul & Barker (2023, hereafter AB23).

In AB22 and AB23, we found that non-linear self-interactions of tidally forced inertial waves induce cylindrical-like differential rotation (also called zonal flows, and also found in Morize et al. 2010; Favier et al. 2014; Cébron et al. 2021, using different kinds of boundary forcing instead of the effective body force in our studies). This differential rotation is particularly strong for thin convective envelopes, high tidal amplitudes (e.g. relevant for tides inside the closest hot Jupiters and stellar binaries) and low viscosities (relevant for the microscopic values in stars and planets), where non-linear effects (including wave–wave and wave–zonal flow interactions and instabilities) were observed to play an important role, as shown in AB2023. In such cases, we have found that non-linear simulations exhibit important deviations from linear predictions for tidal dissipation. In the following, we are particularly interested in exploring the effects of magnetism on the generation of differential rotation and how it modifies tidal dissipation rates in simulations of tidally driven inertial waves in convective envelopes. To do so, we impose an initial (axially aligned) dipolar magnetic field, with a strength that we vary, along with varying the value of the Ohmic diffusivity.

We structure this paper as follows. In Section 2, we describe our magnetohydrodynamical (MHD) model of tidal flows in convective envelopes, including how we drive tidal waves and initialize the magnetic field. We also derive the energetic balances in our model. In Section 3, we describe and analyse the results of our simulations varying the Lehnert number, including exploring the evolution of differential rotation and magnetic field, angular momentum fluxes, and identifying the presence of torsional waves. In Section 4, we vary the magnetic Prandtl number and also examine the occurrence of magnetic instabilities. We present our conclusions, discuss the astrophysical implications of our results and fruitful avenues for further work in Section 5.

2 NON-LINEAR MHD TIDAL MODEL WITH AN INITIAL IMPOSED DIPOLAR MAGNETIC FIELD

We build on the hydrodynamical and non-linear tidal model described in detail in AB22, to which we add an initial dipolar magnetic field. We turn to solving here the MHD equations for tidally excited magneto-inertial waves in an incompressible and adiabatic (neutrally stratified) convective envelope of a low-mass star or giant planet. The size of the inner core (normalized to the total radius R) is fixed to $\alpha = 0.5$, which represents a slightly thicker-than-solar envelope. This value is relevant for modelling lower mass M or K stars throughout certain stages of their evolution, or to a giant planet with an extended dilute core that is sufficiently stably stratified such that it acts like a rigid boundary for low-frequency waves in the convection zone (e.g. Mankovich & Fuller 2021; Pontin et al. 2024). This restriction is made in this initial study of magnetic effects because envelopes with $\alpha = 0.5$ have been the most-widely studied in prior linear and non-linear studies to-date (Ogilvie 2009; Favier et al. 2014; Lin & Ogilvie 2018; Astoul & Barker 2022, 2023). The shell rotates at a frequency Ω_0 along the vertical unit vector $\boldsymbol{e}_z$, and we assume that the envelope consists of fluid with a constant density ρ (which is set to 1, without loss of generality). The momentum,

---

[1] These systems are composed of a Jupiter-like planet orbiting within a few days (typically) around a low-mass star.

induction, and continuity (plus solenoidal constraint on the magnetic field) equations for the tidally excited magneto-inertial waves are given by:

$$\partial_t \boldsymbol{u} + 2\boldsymbol{e}_z \wedge \boldsymbol{u} + (\boldsymbol{u} \cdot \nabla)\boldsymbol{u} = -\nabla p + \mathrm{Le}^2 (\nabla \wedge \boldsymbol{B}) \wedge \boldsymbol{B}$$
$$+ \mathrm{Ek}\,\Delta\boldsymbol{u} + \boldsymbol{f}_t, \tag{1a}$$

$$\partial_t \boldsymbol{B} = \nabla \wedge (\boldsymbol{u} \wedge \boldsymbol{B}) + \mathrm{Em}\,\Delta\boldsymbol{B}, \tag{1b}$$

$$\nabla \cdot \boldsymbol{u} = 0, \tag{1c}$$

$$\nabla \cdot \boldsymbol{B} = 0, \tag{1d}$$

with $\boldsymbol{u}$, $\boldsymbol{B}$, and p the dimensionless velocity, magnetic field, and pressure, and $\Delta = \nabla^2$ the Laplacian operator. We adopt R, Ω_0^{-1}, and B_0 as units of length, time, and magnetic field, respectively, where the latter is a typical strength of the magnetic field. We have introduced several dimensionless parameters, including the Lehnert number $\mathrm{Le} = B_0/(\sqrt{\mu\rho}R\Omega_0)$ (with μ the vacuum magnetic permeability) which is a measure of the magnetic field strength in rotational units (it is the ratio of the rotational time-scale to the Alfvén propagation time-scale over the distance R), and the viscous and magnetic Ekman numbers $\mathrm{Ek} = \nu/(R^2\Omega_0)$ and $\mathrm{Em} = \eta/(R^2\Omega_0)$. In the latter two, ν and η are the (assumed) constant kinematic viscosity and Ohmic diffusivity of the fluid, which can be considered to represent turbulent values (e.g. from mixing-length theories). We also define the magnetic Prandtl number $\mathrm{Pm} = \nu/\eta = \mathrm{Ek}/\mathrm{Em}$, which we vary in our simulations from 10^{-1} to 5, while keeping the Ekman number constant and set to $\mathrm{Ek} = 10^{-5}$. This choice is motivated by mixing-length values for the solar convective envelope (assuming such a turbulent viscosity damps tidal waves, e.g. Ogilvie & Lin 2007; Bekki, Cameron & Gizon 2022, for inertial waves in the Sun), by our previous hydrodynamical simulations that have explored this value extensively (AB22, AB23), and finally by computational limitations that prevent much smaller values of Ek (such as the tiny microscopic ones that are of order 10^{-15} in the solar envelope) from being simulated.

We decompose the tidal flow into an equilibrium/non-wave-like tide and a dynamical/wave-like tide as in AB22 and AB23. The former is assumed to be perfectly maintained on the time-scale of our simulations – which are designed to probe a brief snapshot in the evolution of a system – and to be described within linear theory,[2] but it satisfies the correct tidally perturbed free surface boundary condition at $r = R$ along with the conditions for a rigid core at $r = \alpha R$. This is most directly applicable to modelling the equilibrium tide in a giant planet with a solid core, but it approximately describes the flow in the convective envelope atop a radiative core. The wave-like tide is forced by the effective tidal forcing:

$$\boldsymbol{f}_t = \mathrm{Re}\left\{ -\boldsymbol{e}_z \wedge \nabla \left[\left(r^2 + \frac{2}{3}\alpha^5 r^{-3} \right) Y_2^2(\theta, \varphi) \right] \frac{\omega\, C_t}{1 - \alpha^5} e^{-i\omega t} \right\}, \tag{2}$$

written here in dimensionless units, with (r, θ, φ) and t being spherical polar coordinates and time, Y_2^2 a quadrupolar spherical harmonic, ω the tidal forcing frequency, and C_t the dimensionless tidal amplitude (see also Ogilvie 2013; Lin & Ogilvie 2018). We treat C_t as an input parameter in our study, and this is related to the dimensionless tidal amplitude $\epsilon = (M_2/M_1)(R/a)^3$ by $C_t = (1 + k_2)\epsilon$,

---

[2]It is by definition the quasi-hydrostatic adjustment of a body, and its associated flow, due to the tidal and self-gravitational potentials from the perturber and the perturbed body, respectively (e.g. Ogilvie 2014).

where M_2 and M_1 are the masses of the perturber and perturbed body, respectively, a is the orbital semimajor axis, and k_2 is the real part of the quadrupolar Love number (typically approximated by its hydrostatic value).

Note that equation (2) is purely hydrodynamical, namely, it only takes into account the non-inertial term (i.e. the Coriolis pseudo-force) acting on the equilibrium tide that is omitted from its definition and which is taken to drive tidal waves here. Astoul et al. (2019) have studied how magnetism can modify the equilibrium tide, and thus the excitation of magneto-inertial waves. However, the impact of this magnetic contribution to the tidal forcing is negligible (in the linear regime) compared with equation (2), when considering either the amplitude of large-scale magnetic fields of low-mass stars hosting hot Jupiters (for the tide in the star) or the magnetic field inside a hot Jupiter itself (for the tide in the planet); therefore, we neglect magnetic effects on equilibrium tides in this study.

We follow AB22 and retain the non-linear terms involving tidal waves only, but not those involving the equilibrium tidal flow. As explained in AB22, this is justified if the wavelengths of the waves are much shorter than the radius of the body (and the tidal velocity magnitudes of the waves are larger), which is typically satisfied in our calculations and is usually also expected in reality. Incorporating non-linear interactions with the equilibrium tide in our spherical shell geometry has also been found to lead to unphysical angular momentum evolution (Favier et al. 2014, AB22). The same arguments are expected to hold for the non-linear Lorentz force and magnetic induction terms involving the equilibrium tidal flow with the tidal waves and their magnetic field perturbations. Future work should explore the additional contributions of non-linear interactions with the equilibrium tidal flow in realistic tidally deformed geometries, but performing such studies will be a formidable task.

We adopt stress-free and impenetrable boundary conditions for the velocity of the tidal waves, and current-free (i.e. insulating, $\boldsymbol{e}_r \cdot (\nabla \wedge \boldsymbol{B}) = 0$) boundary conditions for the magnetic field at both the inner and outer shells, where the field also continuously matches onto a potential field in the core and exterior of the body. Note that impenetrable conditions are not applied to the equilibrium tidal flow at the surface, which satisfies the correct free surface condition.

We use the spherical pseudo-spectral code MAGIC to perform MHD simulations of non-linear tidal waves in the presence of magnetic fields (see Section 2.1). In MAGIC, the velocity and magnetic fields are described using a poloidal/toroidal decomposition since they are both solenoidal [equations (1c) and (1d)]. In other words, they can be decomposed as (here for the magnetic field):

$$\boldsymbol{B} = \nabla \wedge (\nabla \wedge g\boldsymbol{e}_r) + \nabla \wedge h\boldsymbol{e}_r, \tag{3}$$

where g and h are poloidal and toroidal scalar potentials, respectively. In the following, we will refer to the poloidal and toroidal magnetic fields as $\boldsymbol{B}_p = \nabla \wedge (\nabla \wedge g\boldsymbol{e}_r)$ and $\boldsymbol{B}_t = \nabla \wedge h\boldsymbol{e}_r$, respectively, with corresponding poloidal and toroidal energies $M_p = \mathrm{Le}^2\langle|\boldsymbol{B}_p|^2/2\rangle$ and $M_t = \mathrm{Le}^2\langle|\boldsymbol{B}_t|^2/2\rangle$, respectively (with $\langle\cdot\rangle$ denoting a volume integral over the whole shell).

Our model and governing equations (equations 1) are similar to those in Lin & Ogilvie (2018), except that we solve the fully non-linear system for magnetic tidal waves whereas they performed linear calculations. We also adopt an initial dipolar magnetic field (rather than a 'background field' as in Lin & Ogilvie 2018, but of the same form, with opposite sign):

$$\boldsymbol{B}(t = 0) = \boldsymbol{B}_0 = -\left(\frac{\alpha}{r}\right)^3 \left[\cos\theta\, \boldsymbol{e}_r + \frac{\sin\theta}{2}\boldsymbol{e}_\theta\right], \tag{4}$$

which has dimensional amplitude B_0. Thus, initially, the magnetic energy in the whole shell of volume V is:

$$M_0 = \text{Le}^2 \int_V \frac{|\boldsymbol{B}_0|^2}{2} r^2 \sin\theta \, dr \, d\theta \, d\varphi = \alpha^3 \text{Le}^2 \frac{\pi}{3} \left(1 - \alpha^3\right). \quad (5)$$

The magnetic field $\boldsymbol{B}_0$ is allowed to evolve, but it is not self-sustained by convective motions, so it will decay Ohmically. We define a new Lehnert number which follows the evolution of the poloidal magnetic field $M_p(t)$:

$$\text{Le}_p(t) = \sqrt{\frac{3 M_p}{\alpha^3 \pi \left(1 - \alpha^3\right)}}, \quad (6)$$

such that $\text{Le}_p = \text{Le}$ at $t = 0$, where M_p is the poloidal magnetic energy (with $M_p = M_0$ at $t = 0$). We also define a corresponding toroidal Lehnert number, which takes a similar form: $\text{Le}_t(t) = \sqrt{3 M_t / \left[\alpha^3 \pi \left(1 - \alpha^3\right)\right]}$, where $\text{Le}_t(t = 0) = 0$ initially.

The sum of the integrated magnetic ($M = \text{Le}^2 \langle |\boldsymbol{B}|^2 \rangle / 2 = M_p + M_t$) and kinetic ($K = \langle |\boldsymbol{u}|^2 \rangle / 2$) energies satisfies the energetic balance described by:

$$\partial_t (M + K) = P_t + \mathcal{F}_P - D_\nu - D_\eta. \quad (7)$$

This can be derived using equations (1) and the boundary conditions. When our simulations reach an overall steady state, the rate of energy injected by the tide, i.e. the tidal power, defined by $P_t = \langle \boldsymbol{u} \cdot \boldsymbol{f}_t \rangle$, is mostly balanced by the sum of viscous and Ohmic dissipation, $D_\nu = -\langle \text{Ek} \, \boldsymbol{u} \cdot \Delta \boldsymbol{u} \rangle$ and $D_\eta = -\langle \text{Le}^2 \text{Em} \, \boldsymbol{B} \cdot \Delta \boldsymbol{B} \rangle$. The Poynting flux $\mathcal{F}_P = \text{Le}^2 \int_{\delta V} \boldsymbol{u} \cdot \boldsymbol{B} \, B_r \, dS$, quantifies the transfer of magnetic energy through the inner and outer boundaries, but this is almost always found to be negligibly small in our simulations (see also Anufriev, Jones & Soward 2005) so can be ignored for our purposes.[3] Furthermore, the total angular momentum is conserved in the simulations given our choice of boundary conditions for the magnetic field and velocity, following appendix A of Jones et al. (2011), combined with the fact that the effective wave-like tidal torque $\boldsymbol{r} \wedge \boldsymbol{f}_t \propto e^{2i\phi}$ also vanishes when integrating over the whole shell (see AB22 for further details of the latter). We have verified that both energetic and angular momentum balances are accurately satisfied in our simulations, as we will discuss further below.

As in Favier et al. (2014), AB22, and AB23, we also define the mean rotation rate of the fluid, relative to the reference frame rotating at the rate Ω_0, by $\delta\Omega = \langle u_\varphi / (r \sin\theta) \rangle / V$, where V is the fluid volume, and the energy in the differential rotation $E_{dr} = \langle \left(\langle u_\varphi \rangle_\varphi - \delta\Omega \, r \sin\theta\right)^2 \rangle / 2$, where $\langle \cdot \rangle_\varphi$ denotes a φ-average. Note that $\delta\Omega$ can be non-zero despite global angular momentum conservation, as a result of differential rotation produced within the fluid volume, though it is typically quite small. The energy in differential rotation E_{dr} is helpful in quantifying the generation of zonal flows by non-linear self-interactions of tidal waves.

2.1 Magic code and ranges of parameter values

We solve the system of equations (1) with the 3D pseudo-spectral MHD code Magic,[4] (version 6.2). We set the Ekman number to Ek $= 10^{-5}$, the radial aspect ratio to $\alpha = 0.5$, the tidal frequency

Table 1. Values of the Lehnert number Le at different ages in a $1 \, M_\odot$ star at the base (BCZ) and the top (TCZ) of the convective envelope for slow and fast initial rotation from Astoul et al. (2019). These values adopt the magnetostrophic regime to estimate a mean magnetic field (this is likely to provide an upper limit on Le and agrees best with observations for low-mass stars over other scaling laws discussed in Astoul et al. 2019).

| Zone	BCZ		TCZ	
Age \ initial rotation	Slow	Fast	Slow	Fast
PMS ($t \sim 10^7$ yr)	10^{-2}	4×10^{-3}	2×10^{-3}	8×10^{-4}
Beg. MS ($t \sim 10^9$ yr)	2×10^{-2}		4×10^{-3}	
End MS ($t \sim 10^{10}$ yr)	4×10^{-2}		5×10^{-3}	

to $\omega = 1.1$ (motivated by former studies as discussed for the aspect ratio in the beginning of Section 2), and finally the tidal forcing amplitude $C_t = 10^{-2}$, unless otherwise stated. This choice allows us to explore the impact of magnetism on tidal flows in the convective shell for a tidal frequency relevant for inertial wave excitation, and we explore variations in the Lehnert number Le in the range $[10^{-5}, 1]$, and the magnetic Prandtl number Pm in the range $[10^{-1}, 5]$. The range of Le covers weakly magnetized cases with Le $= 10^{-5}$ and cases that are strongly magnetized with Le $\gtrsim 0.1$. It can be compared with the range Le $\in [10^{-4}, 10^{-1}]$ computed in solar-type convective envelopes from the pre-main sequence (PMS) to the end of the main sequence (MS) by Astoul et al. (2019) using a 1D stellar evolution code and scaling laws to estimate the overall amplitude of the magnetic field, as reported in Table 1 for $M = 1 \, M_\odot$.[5] Le increases as the star gets older, mainly because the star slows down its rotation. Smaller values with Le $\lesssim 10^{-4}$ are expected in giant planets like Jupiter (using values, and the magnetostrophic scaling law that is likely to provide an upper bound, in e.g. Wahl et al. 2017; Astoul et al. 2019), and Le $\lesssim 10^{-3}$ in spin-synchronized hot Jupiters (also using values from fig. 11 of de Vries, Barker & Hollerbach 2023). Realistic values of Pm in stars are typically $\mathcal{O}(10^{-2})$ using microscopic diffusion coefficients, and can be even smaller in giant planets (even $\mathcal{O}(10^{-5})$, e.g. French et al. 2012, where Em can be estimated between 10^{-13} and 10^{-11} in the convective region of a Jupiter-like model). However, if Ek is considered to represent a turbulent viscosity in mixing-length theory, we might expect η to also represent a turbulent value, in which case Pm may be $O(1)$ (e.g. Käpylä et al. 2020). Note that $C_t = 10^{-2}$ is the approximate value for the tide in a hot Jupiter orbiting a solar-type star in one day, or for the tide in a solar-type binary star also with an orbital period of one day.

Our simulations are usually run for times $t \gtrsim 10\,000$, corresponding to more than 0.1 global viscous times, which is usually sufficient to reach a time-averaged steady state (for the tidal power and dissipation, although the magnetic field continues to slowly decay). We use a CNAB2 scheme[6] for time integration with an adaptive time-step (dt) satisfying a Courant–Friedrichs–Lewy condition, which is no larger than $dt = 10^{-2}$ to guarantee adequate time resolution. We adopt a Chebyshev collocation method in the radial direction and spherical harmonics in the horizontal directions in Magic. The spatial resolution used in the simulations varies from case to case, from

---

[3]It is strictly non-zero, taking the value $\mathcal{F}_P \approx -2.18 \times 10^{-6}$ in linear theory for a fixed field with strength Le $= 10^{-2}$ with our default parameters. This is much smaller than the corresponding $D_\nu \approx 3.5 \times 10^{-3}$ (and $D_\eta \approx 9.31 \times 10^{-4}$).

[4]https://magic-sph.github.io/

[5]Values of Le are found to be of the same order of magnitude for other masses with $M = 0.6$, 0.8, and $1.2 \, M_\odot$.

[6]It is a second-order scheme assembled from the combination of a Crank-Nicolson for the implicit terms (i.e. for the Coriolis and non-linear terms) and a second-order Adams-Bashforth for the explicit terms (i.e. for the others linear terms) in the governing wave equations.
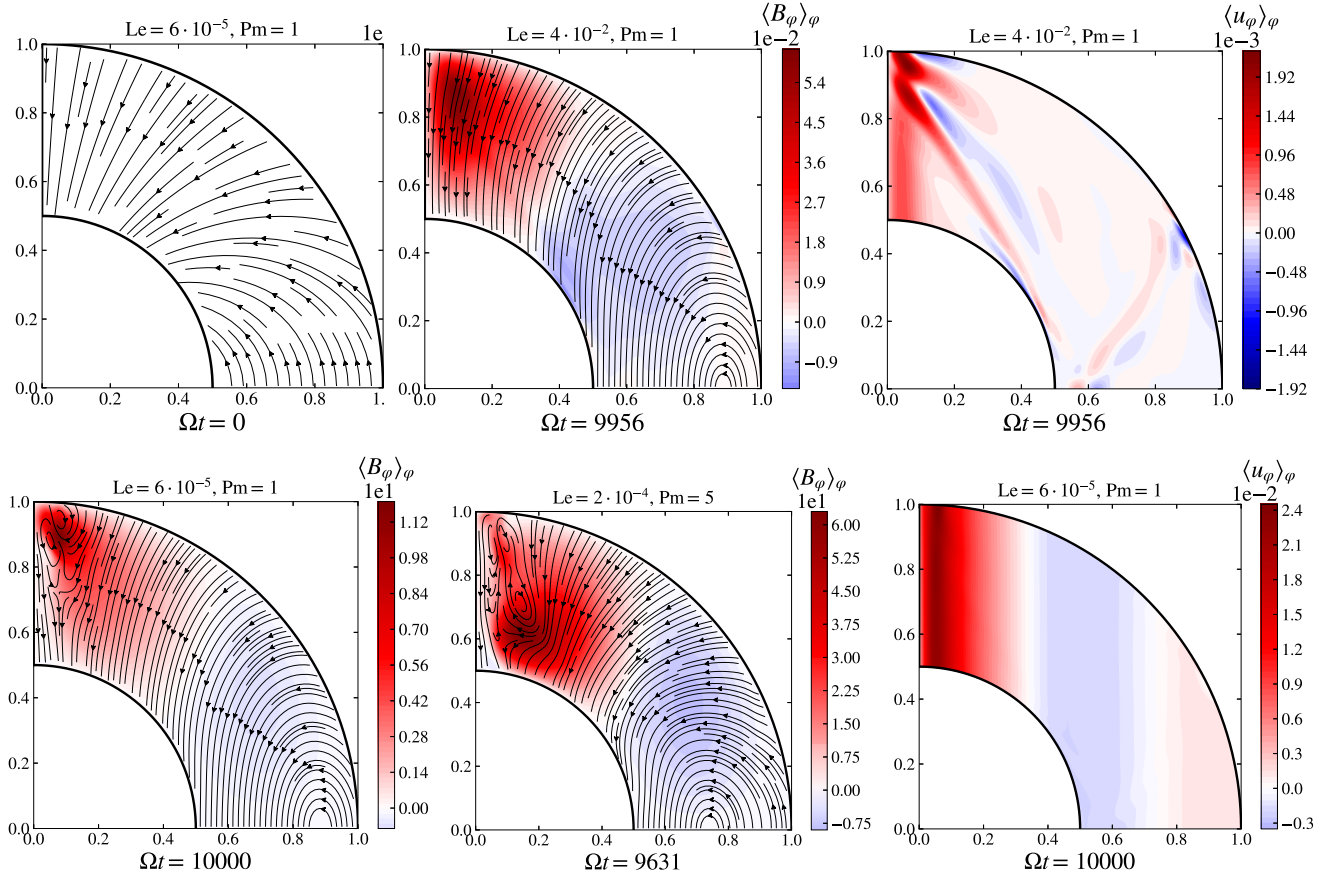
Figure 1. First and second columns: meridional, in the (r, θ) plane, magnetic field lines (in black, with arrows), along with the azimuthally averaged azimuthal magnetic field, $\langle B_\varphi \rangle_\varphi$, at $t = 0$ (top left) and at the times indicated in three different simulations. $\langle B_\varphi \rangle_\varphi$ is predominantly antisymmetric about the equator so we have only plotted one quadrant. Upper left: initial dipolar magnetic field lines in all simulations. Right column: azimuthally averaged azimuthal velocity (symmetric about the equator) $\langle u_\varphi \rangle_\varphi$ in two simulations at the times indicated. The zonal flow for Pm = 5, Le = 2×10^{-4} cannot be distinguished from the flow shown here for Le = 6×10^{-5}, Pm = 1 (that is why the former is not shown here).

$n_{r,\mathrm{max}} = 97$ (number of radial gridpoints), $l_{\mathrm{max}} = 213$ (maximum spherical harmonic degree), and $m_{\mathrm{max}} = 10$ (maximum spherical harmonic order) for the less demanding simulations at low Lehnert numbers Le, up to $n_{r,\mathrm{max}} = 193$, $l_{\mathrm{max}} = 341$, and $m_{\mathrm{max}} = 100$ for the more demanding simulations at high Le and/or high magnetic Prandtl numbers Pm. To guarantee adequate (horizontal and radial) spatial resolution, we used an empirical 'rule of thumb' that ensures that there is at least 3 orders of magnitude of difference between the peak of the energy spectrum and the energy in the highest resolvable wavenumbers, both for horizontal (spherical harmonic degree ℓ and azimuthal order m) and radial directions (in terms of Chebyshev spectral coefficients) when the simulation reaches an approximate steady state.

3 NUMERICAL RESULTS VARYING Le FOR Pm = 1

Our simulations begin with an aligned dipole field (equation 4) in the absence of flow, with the tidal forcing being switched on at $t = 0$. Tidal waves are excited and subsequently interact with the magnetic field, which gradually decays on a long time-scale because of Ohmic diffusion. The resulting dynamics is due to a competition between tidal forcing, hydrodynamic non-linearity, and viscous damping, as well as the interaction of tidal flows with the magnetic field through

Lorentz forces, and the modification of the field by both the flows and Ohmic diffusion. We are particularly interested in the effects of the field on tidal flows (both tidal waves and zonal flows) – and the modifications of the resulting tidal dissipation with magnetic fields – but also in studying the modification of the field by the tidal flows.

3.1 Evolution of the magnetic field and differential rotation for weaker fields

We first explore the impact of a weak dipolar magnetic field on tidal wave-like flows, setting the initial Lehnert number Le $\in [10^{-5}, 10^{-3}]$ and Pm = 1. The initial dipolar magnetic field lines in the meridional plane are shown in the top-left panel of Fig. 1, with the other panels in this figure showing the meridional (equivalently axisymmetric poloidal) magnetic field lines and mean azimuthal components at the specified times in simulations with different Le, together with examples of the zonal flows in the right panels (a weak field case in the bottom-right panel and a strong field case in the top-right). In Fig. 2, we display the evolution of the poloidal and toroidal components of the magnetic energy, normalized by the initial squared Lehnert number. For early times $t \lesssim 500$, the magnetic field is primarily poloidal (as imposed by the initial conditions), before a toroidal component grows and becomes dominant. The latter is produced by the cylindrical differential rotation (zonal flows) – created by non-
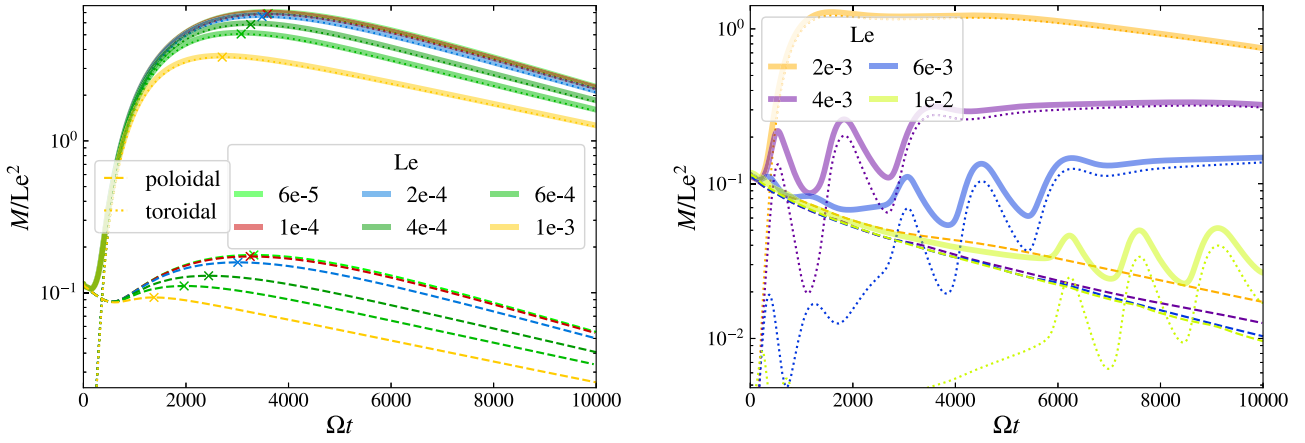
Figure 2. Total, poloidal, and toroidal magnetic energy normalized by the Lehnert number squared (M/Le^2) for $\mathrm{Pm} = 1$ in solid, dashed, and dotted lines, respectively. Each cross indicates a local maximum of either the poloidal or toroidal magnetic energy for each simulation. Left: for low initial Lehnert numbers for which the tidally driven zonal flow is not destroyed. Right: for higher initial Lehnert numbers for which the tidally driven zonal flow is inhibited even shortly after the start of the simulation.
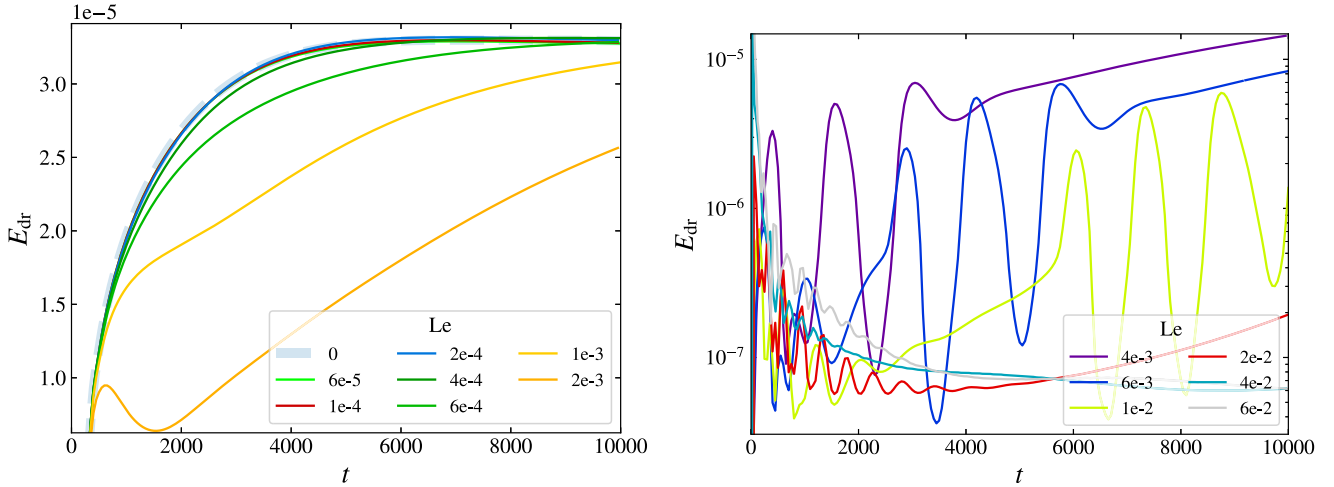
Figure 3. Energy in the differential rotation E_{dr} against time for low (left) to high (right) initial Lehnert numbers Le (in different colours). The hydrodynamical evolution of E_{dr} (i.e. for $\mathrm{Le} = 0$) is indicated in the pale dashed line in the left plot for reference.

linear self-interactions of inertial waves (see Tilgner 2007; Favier et al. 2014, AB22) – stretching poloidal field lines, i.e. by the so-called Ω-effect (e.g. Moffatt 1978; Spruit 1999) which we explore in detail below. The differential rotation is found to be stronger for weaker magnetic fields, as we observe in the left panel of Fig. 3. This figure shows the energy in the differential rotation E_{dr} and its tendency to evolve towards the hydrodynamical value ($\mathrm{Le} = 0$) for smaller Le. For simulations with $\mathrm{Le} \leq 2 \times 10^{-3}$, these zonal flows efficiently stretch the poloidal magnetic field lines to produce a toroidal magnetic field, as is shown (in colour) in the bottom-right (zonal flow) and bottom-left (toroidal field) panels of Fig. 1.

Since the tidally driven zonal flow (shown in the bottom-right panel of Fig. 1) is axisymmetric and mainly independent of the vertical coordinate z (along the rotation axis), we can write it as $\boldsymbol{U}(s) = \langle u_\varphi \rangle_{z,\varphi} \boldsymbol{e}_\varphi = s\delta\Omega(s)\boldsymbol{e}_\varphi$ with $s = r\sin\theta$ the cylindrical radius, and where the azimuthal velocity is vertically and azimuthally averaged. By ignoring Ohmic diffusion in equation (1b), the interaction of the initial magnetic field $\boldsymbol{B}_0$ with the zonal flow induces an axisymmetric

toroidal magnetic field $\boldsymbol{B}_\Omega$ satisfying:

$$\partial_t \boldsymbol{B}_\Omega = \nabla \wedge (\boldsymbol{U} \wedge \boldsymbol{B}_0)$$

$$= \boldsymbol{e}_\varphi s(\boldsymbol{B}_0 \cdot \nabla)\delta\Omega(s) = \frac{3}{2}B_0^r s \sin\theta \, \boldsymbol{e}_\varphi \partial_s \delta\Omega(s), \qquad (8)$$

using $B_0^r = -\left(\frac{\alpha}{r}\right)^3 \cos\theta = 2B_0^\theta \cot\theta$ from equation (4). It is not straightforward to verify this quantitatively in simulations in which the tidally driven zonal flow first develops before winding up the initial magnetic field. Thus, we have tested this mechanism by also restarting a hydrodynamical simulation (described in AB22) with a steady zonal flow with $\omega = 0.2$ (for which we had suitable hydrodynamical data, but the mechanism is the same for $\omega = 1.1$ except that the zonal flows take a different form) and $C_t = 5 \times 10^{-2}$, by injecting a dipolar magnetic field (equation 4) and solving equation (1) from an initial time (relative to the hydrodynamic initial state) $t = 10\,000$. From the φ-averaged snapshots shown in Fig. 4, it is clear that the Ω-effect explains the amplitude and the structure of the azimuthal magnetic field early in the simulation. The snapshot
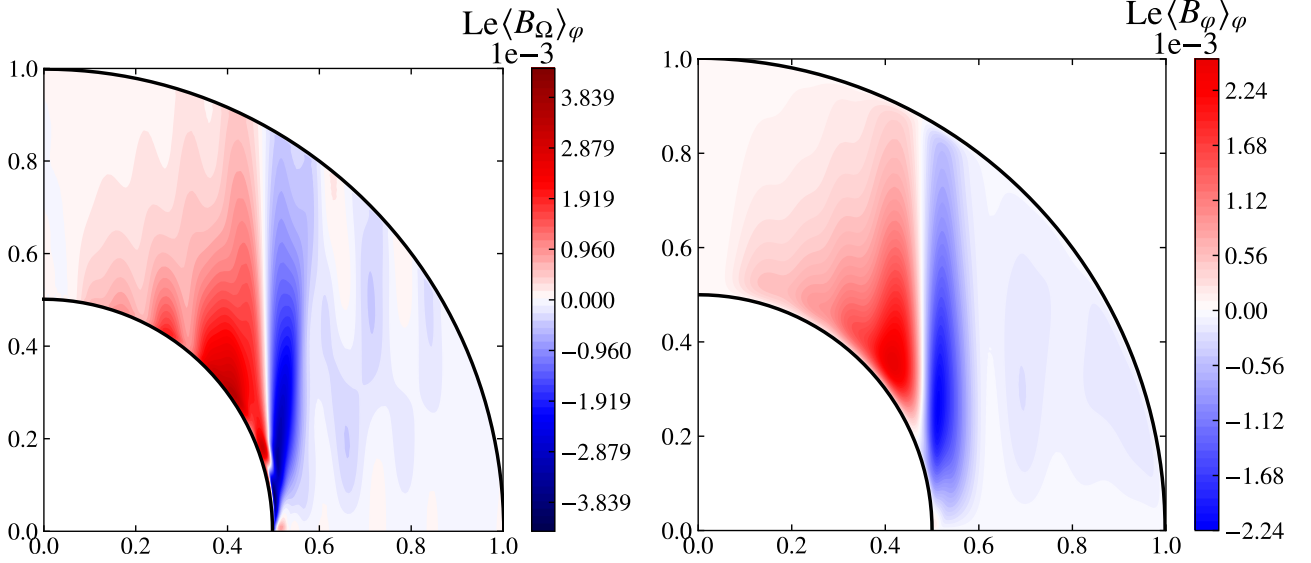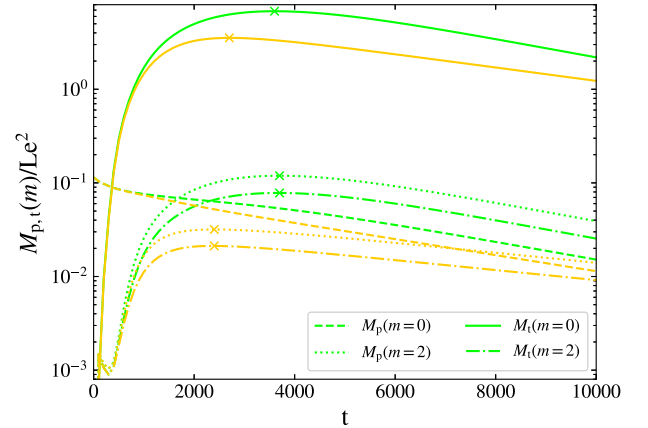
Figure 4. Azimuthal average of the toroidal magnetic field produced by predictions of the Ω-effect $\langle B_\Omega \rangle_\varphi$ (left) and azimuthal magnetic field $\langle B_\varphi \rangle_\varphi$ (right) at $t = 1050$ from the outputs of a hydrodynamical simulation (from AB22) restarted at $t = 10^4$ with an initial dipolar magnetic field with Le $= 10^{-3}$, Pm $= 2$, and $\omega = 0.2$. Left: $\langle B_\varphi \rangle_\varphi$ computed using the right-hand side of equation (8), $\times 50$ for time integration. Right: the colour range shown is the same as in the left panel (though the values taken slightly differ).

after 50 rotation periods (right panel) matches quite well with the prediction $\boldsymbol{B}_\Omega$ derived from equation (8).

The time taken for differential rotation to build up a toroidal magnetic field of the same magnitude as the poloidal magnetic field can be estimated from equation (8). We refer to it as the winding-up time, similarly as in Aurière et al. (2007) and Jouve, Gastine & Lignières (2015):

$$t_\Omega = \left(\frac{\partial \delta\Omega}{\partial \ln s} \right)^{-1}. \qquad (9)$$

Note that, since the differential rotation becomes strong close to the poles in our simulations, $\sin\theta$ (in equation 8) differs substantially from one, reducing the right-hand side by almost an order of magnitude. Taking into account this reduction, we estimate this time-scale (early in the simulation) to be $t_\Omega = \mathcal{O}(10)$ in the restarted hydrodynamic case for Le $= 6 \times 10^{-5}$ and $t_\Omega = \mathcal{O}(100)$ in other simulations for Le $\lesssim 2 \times 10^{-2}$. These are consistent with the times where $M_p = M_t$ (see e.g. Fig. 2). After that (for $t \gtrsim 500$), the poloidal magnetic energy increases, possibly due to the $m = 2$ wave-like flow stretching the newly created axisymmetric toroidal magnetic field, as suggested in Appendix B and by Fig. 1 (bottom-left panel), where poloidal magnetic field lines are significantly modified close to the poles where the toroidal magnetic field is strong. The resulting poloidal magnetic field should then have a quadrupolar component, which is strongly corroborated by Fig. 5 that depicts evolution of the dominant magnetic energy components.[7] Indeed, we observe a strong increase in $M_p(m = 2)$ and $M_t(m = 2)$ shortly after $t \sim 500$. Similarly, the rise of the latter may result from the action of the tidal flow on $\boldsymbol{B}_p(m = 0)$. From $t = 1700$, the amplitude of $M_p(m = 2)$ for Le $= 6 \times 10^{-5}$ exceeds that of $M_p(m = 0)$ (which is decaying),

---

[7]The next strongest component $m = 4$ (due to superharmonics at 2ω, Astoul & Barker 2022) is at least one order of magnitude lower than $m = 0$ or 2 throughout these simulations.


Figure 5. Evolution of the poloidal and toroidal magnetic energies M_p and M_t (normalized by Le^2) for various azimuthal wavenumber components, the $m = 0$ (axisymmetric) and $m = 2$ (non-axisymmetric) components, for two simulations with Le $= 6 \times 10^{-5}$ (in green) and Le $= 10^{-3}$ (in yellow). Crosses indicate maxima.

and peaks at $t = 3700$ (as does $M_t(m = 2)$), later than $M_t(m = 0)$ which peaks around $t = 3600$, supporting our inference that the wave-like flow $\boldsymbol{u}_w(m = 2)$ acts on $\boldsymbol{B}_\Omega$ to create $\boldsymbol{B}_p(m = 2)$. As a result, after a few thousand rotation units, the poloidal magnetic energy is dominated by its quadrupolar component. This observation, coupled with the fast decay of $M_p(m = 0)$, explains why the total poloidal magnetic energy $M_p \approx M_p(m = 0) + M_p(m = 2)$ increases and reaches a maximum earlier, around $t = 3300$ in Fig. 2, while M_t, which is dominated by its axisymmetric component from the beginning, peaks later, still around $t = 3600$.

It is difficult to predict the maximum amplitude reached by the axisymmetric toroidal magnetic field, especially in simulations where both magnetism and differential rotation are evolving on similar time-

scales.[8] The saturation of the toroidal magnetic field amplitude could result from a complex interplay between Ohmic diffusion, magnetic tension from the Lorentz force (this is very weak for $\mathrm{Le} = 6 \times 10^{-5}$ but is appreciable for larger Le) and the production of axisymmetric and quadrupolar poloidal and toroidal components of the magnetic fields. We estimate the shear length-scale (i.e. the length-scale over which the rotation varies substantially) close to the poles, where the zonal flow is produced, to be

$$l_\Omega = (\partial \ln \Omega / \partial s)^{-1}, \tag{10}$$

which takes the value $l_\Omega = \mathcal{O}(10^{-1})$ for $\mathrm{Le} \lesssim 10^{-3}$, where $\Omega = 1 + \delta\Omega$. For this length-scale, the Ohmic diffusion time-scale is $t_\eta = l_\Omega^2 / \mathrm{Em} = \mathcal{O}(10^3)$, which is on the same order as the time-scale for the saturation of the magnetic field. However, the root mean square (RMS) amplitude of the Ohmic diffusion term is one order of magnitude lower than the RMS induction terms in equation (1b), so Ohmic diffusion is unlikely to be solely responsible for saturating M_t.

On the other hand, the Alfvén time-scale, which quantifies the time taken for magnetic perturbations to propagate energy out of the shear region (defined later), varies from $t_{ap} \sim 10^5$ ($t_{ap} \sim 10^4$) for $\mathrm{Le} = 10^{-5}$, to $t_{ap} \sim 10^3$ ($t_{ap} \gtrsim 10^2$) for $\mathrm{Le} = 10^{-3}$, down to $t_{ap} \gtrsim 10$ ($t_{ap} \gtrsim 10$) for $\mathrm{Le} = 6 \times 10^{-2}$ when estimated at $t \approx 100$ (at $t \approx 500$). It will be shown that t_{ap} is relevant to explain the transition between regimes with strong or magnetically inhibited zonal flows, but it is too long to explain the saturation of M_t occurring at a few thousand rotation units in simulations with low Lehnert numbers. Moreover, we have to account for decay of the poloidal magnetic field due to Ohmic diffusion, and for the newly created toroidal magnetic field $\boldsymbol{B}_\Omega$ being converted into $B_p(m=2)$ by the stretching effects of the quadrupolar tidal flow (as explained before and in Appendix B). These additional effects may reduce overall production of toroidal magnetic energy. Finally, the evolution of the strength of the zonal flow, with a peak of E_{dr} around $t = 7000$ for $\mathrm{Le} = 6 \times 10^{-5}$ (see Fig. 3), is also likely to play a role. In the restarted hydrodynamical simulation, where the zonal flow is nearly steady, both poloidal and toroidal magnetic energies saturate a bit sooner (after 2000 rotation units) than in the non-restarted simulations (after nearly 4000 rotation units).

As we decrease the initial Lehnert number, magnetic energies converge towards an asymptotic limit that seems to be reached for $\mathrm{Le} \approx 6 \times 10^{-5}$, with magnetic energy evolutions for lower Le being identical when rescaled by Le^2 (omitted from the figure). This implies a kinematic regime for low enough Lehnert numbers, in which the role of Lorentz forces becomes negligible and the tidal flow is not affected by the magnetic field any more. In this regime, the induction equation is linear in $\boldsymbol{B}$. This kinematic effect of the tidal flows on the magnetic field is further supported by Fig. 6, which shows the relationship between the RMS toroidal and poloidal magnetic fields (equation 6) as they evolve in time in each simulation. The simulations for low Lehnert number $\mathrm{Le} \leq 10^{-3}$ are first dominated by the Ω-effect due to stretching of the poloidal field by differential rotation (vertical increase of Le_t in Fig. 6) and by advection of the newly created azimuthal field by the tidal flow to a lesser extent (slight horizontal bend toward higher Le_p until a maximum is reached). The maximum toroidal magnetic field is approximately six times larger than the maximum poloidal magnetic field, given by the ratio
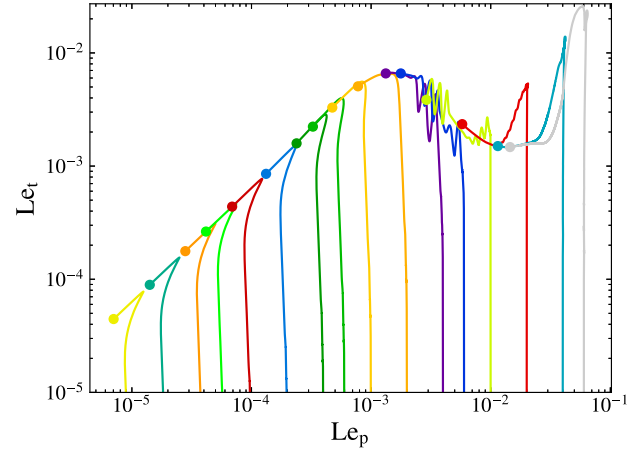
Figure 6. $\mathrm{Le}_t(t)$ versus $\mathrm{Le}_p(t)$ for simulations with $\mathrm{Pm} = 1$ having different initial Lehnert numbers Le (with $\mathrm{Le}_p(t = 0) = \mathrm{Le}$) in different colours. Bullet points indicate the values reached at the end of each simulation. The left of the figure where $\mathrm{Le}_t \propto \mathrm{Le}_p$ indicates a kinematic regime where Lorentz forces are weak.

$\mathrm{Le}_t/\mathrm{Le}_p$. Once this value is reached and the differential rotation attains a steady state, Le_t just decays linearly due to Ohmic diffusion, i.e. $\mathrm{Le}_t \propto \mathrm{Le}_p$ for $\mathrm{Le} \leq 10^{-3}$.

In our simulations, which do not model turbulent convective motions and the resulting dynamos, the magnetic field is not self-sustained. Hence, in the absence of fluid motions substantially maintaining (or amplifying) the field, magnetic energy is expected to decay due to Ohmic diffusion, approximately according to

$$\partial_t M = -\mathrm{Le}^2 \mathrm{Em} \langle (\nabla \wedge \boldsymbol{B})^2 \rangle = -D_\eta, \tag{11}$$

when the induction term $\nabla \wedge (\boldsymbol{u} \wedge \boldsymbol{B})$ is neglected. Using a poloidal/toroidal decomposition of the magnetic field, we can solve the induction equation to find freely decaying modes (as in Appendix A, following Moffatt 1978). For the single largest radial wavelength $l = 1$ mode, we predict a decay rate for the poloidal magnetic energy (i.e. for $-\mathrm{d} \ln M_p / \mathrm{d}t$) of approximately 1.79×10^{-4}. This is quite close to the observed decay rate for the same component of the magnetic energy, which we measure to be 2.1×10^{-4} in the last thousand time units for[9] $\mathrm{Le} \in [10^{-5}, 6 \times 10^{-2}]$. Since we observe the same decay for a comparison simulation with a lower tidal forcing amplitude $C_t = 10^{-4}$, we can rule out tidal flows acting to enhance Ohmic decay, which could in principle explain the small difference in values by producing smaller magnetic length-scales. Similar values, but one order of magnitude higher, are found when $\mathrm{Pm} = 0.1$. For simulations with $\mathrm{Pm} = 2$ and 5, the predicted decay rates are, respectively, 8.96×10^{-5} and 3.59×10^{-5}, while the measured decay rates are again slightly higher, $\sim 1.1 \times 10^{-4}$ and $\sim 6 \times 10^{-5}$, respectively. The small discrepancies between predicted and observed values could come from the initial dipole not being a single free decay eigenmode. It can be represented as a sum of free decay eigenmodes (with different k_α's, using the notation of Appendix A), since the set of these forms an orthogonal basis for a single l, m. Thus, we would not expect a single free decay eigenmode to exactly explain the observed decay rate because the field in our simulations is a superposition of these with different decay rates.

---

[8]For comparison, we observe that in the restarted hydrodynamical simulation with $\omega = 0.2$, the maximum toroidal magnetic energy is twice the maximum of M_t taken in the non-restarted simulation for $\mathrm{Le} = 6 \times 10^{-5}$.

[9]We measure the same decay for a simulation with $\mathrm{Le} = 10^{-3}$ running until 40 000.
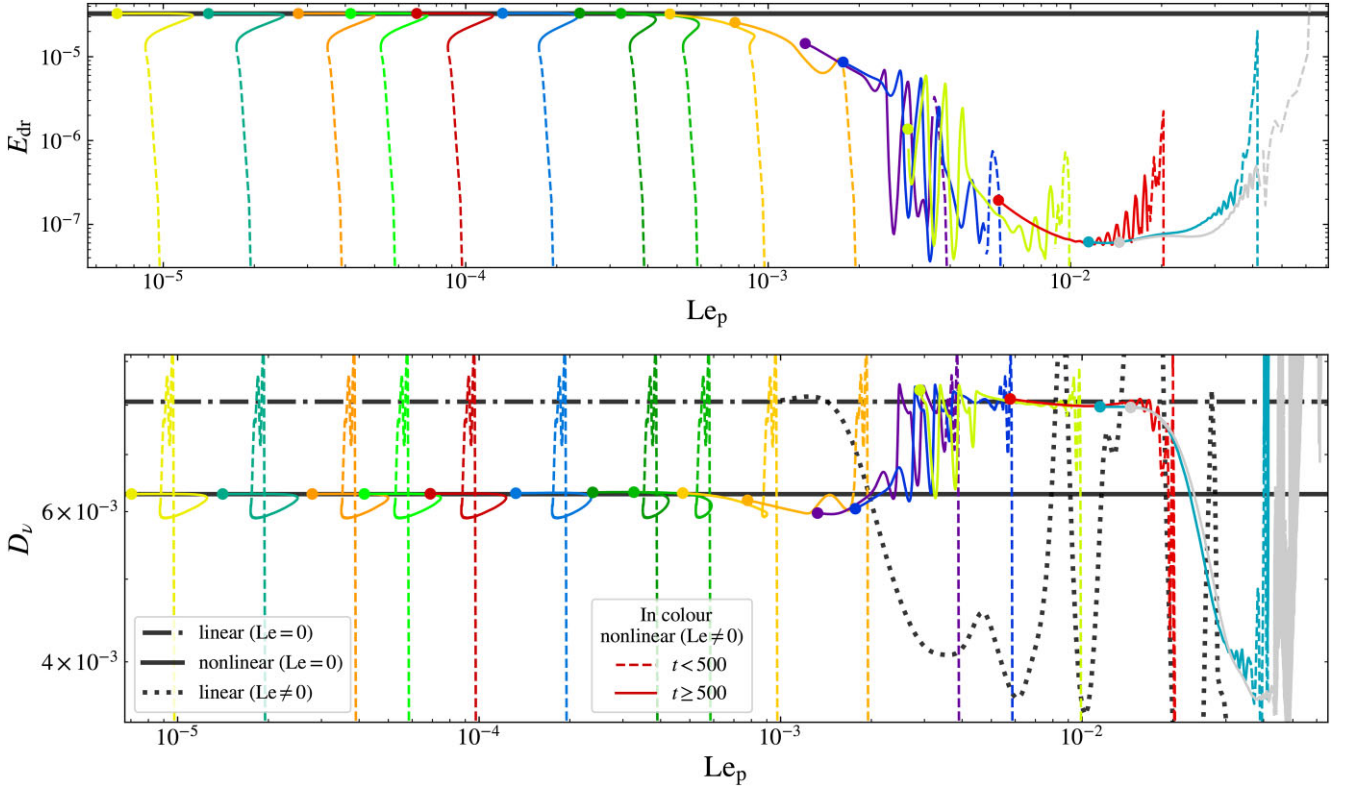
Figure 7. Energy in differential rotation E_{dr} (top) and viscous dissipation D_ν (bottom) against the poloidal Lehnert number Le_p for $Pm = 1$ and $Ek = 10^{-5}$. Non-linear MHD simulations are shown in colour (non-black), each colour referring to a simulation with a different initial Lehnert number Le (with $Le_p(t = 0) = Le$). Dots indicate the values reached at the end of the simulation around $t = 10^4$. Dashed lines become solid for $t \geq 500$ to indicate the evolution in time. For comparison, linear (magneto-)hydrodynamical predictions (black dotted and black dash–dotted lines) and non-linear hydrodynamical predictions (black solid lines) have been added.

Nevertheless, the approximate agreement between predicted and observed values indicates that in most of our simulations the field is decaying Ohmically, and is not being sustained by, or subject to enhanced (turbulent) diffusion by, the tidal flows.

3.2 Evolution for stronger fields, angular momentum fluxes, and torsional waves

For higher initial Lehnert numbers $Le \gtrsim Le_c$, where $Le_c = 3 \times 10^{-3}$ is a critical value indicating a change of regime, the differential rotation becomes substantially inhibited by the stronger initial magnetic fields within the first thousand time units. This difference between stronger field cases and those with $Le \lesssim Le_c$ is demonstrated particularly clearly by comparing the bottom (small Le) and top (large Le) right panels of Fig. 1. In the latter, polar zonal flows are substantially weaker and the net azimuthal flows are strongest in the (magneto-)inertial wave shear layers instead. The evolution of the differential rotation is also shown in the right panel of Fig. 3 (and in the upper panel of Fig. 7) where E_{dr} is observed to be smaller by more than two orders of magnitude for $Le \sim 10^{-2}$ compared to $Le \lesssim 10^{-3}$. As a result of the correspondingly weaker Ω-effect, the toroidal magnetic energy is also reduced, as is evidenced by the 2D snapshots in Fig. 1 (when comparing the overall amplitude of $\langle B_\varphi \rangle_\varphi$ in the top-middle panel with the bottom-left panels), and also in volume-integrated energies in Fig. 2 (right panel) and Fig. 6. For the largest Le, the poloidal magnetic energy becomes dominant over the toroidal one throughout these simulations.

To better understand what causes the transition between regimes in which tidally driven zonal flows develop strongly or not, we derive an equation governing evolution of angular momentum. We take the azimuthal component of the momentum equation in cylindrical coordinates, multiplied by the cylindrical radius s, to obtain:

$$\partial_t(s\widehat{u_\varphi}) + \frac{1}{s}\partial_s(s\mathcal{F}_s) + \partial_z\mathcal{F}_z = 0, \tag{12}$$

where the $\widehat{}$ symbol denotes the combination of taking a φ-average, z-integration, and time integration (over an arbitrary time τ), such that for a variable A, $\widehat{A} = \int^\tau \int_{z_i}^{z_o} \langle A \rangle_\varphi \, dz \, dt$, with z_i and z_o the inner and outer vertical heights of the spherical boundaries which depend on s. In equation (12), we have introduced the cylindrical radial angular momentum flux

$$\mathcal{F}_s = s\left[-Ek\, s\partial_s(\widehat{u_\varphi}/s) + \widehat{u_s}\widehat{u_\varphi} + \widehat{u_s' u_\varphi'} - Le^2\widehat{B_s B_\varphi} - Le^2\widehat{B_s' B_\varphi'}\right], \tag{13}$$

and the vertical angular momentum flux

$$\mathcal{F}_z = s\left[-Ek\, s\partial_z(\widehat{u_\varphi}/s) + \widehat{u_z}\widehat{u_\varphi} + \widehat{u_z' u_\varphi'} - Le^2\widehat{B_z B_\varphi} - Le^2\widehat{B_z' B_\varphi'}\right]. \tag{14}$$

In these, we define the prime $'$ symbol to denote non-axisymmetric fluctuations to distinguish them from axisymmetric ones, such that $u_i = \langle u_i \rangle_\varphi + u_i'$ (since $\langle u_i' \rangle_\varphi = 0$). In both fluxes, from left to right, we have the contributions from viscous diffusion (VD), meridional circulations (MC), Reynolds stresses (RS), magnetic torques (MT), and Maxwell stresses (MS, similarly as in Brun 2004; Browning 2008, in spherical coordinates). Here, the MT (MC)
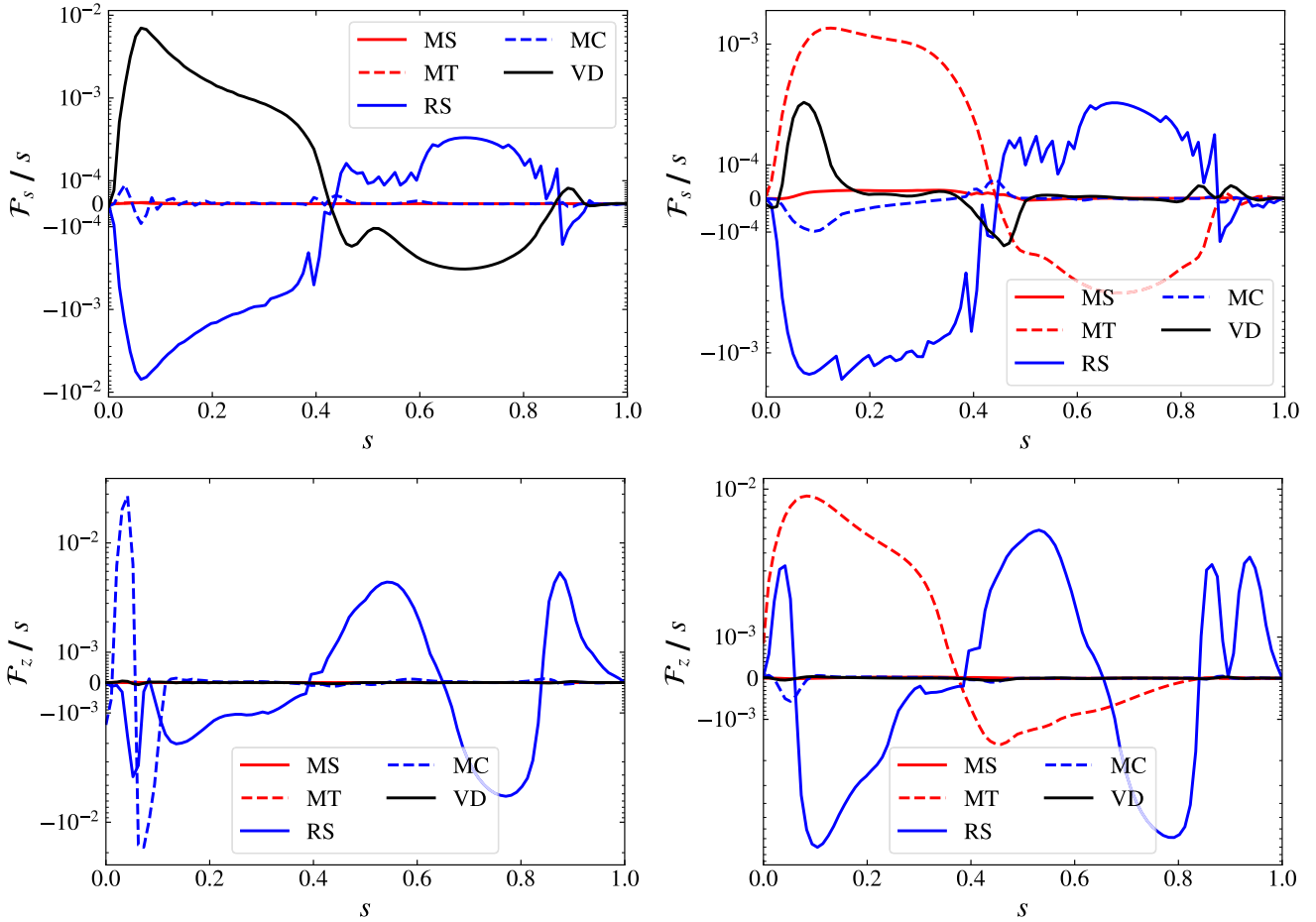
Figure 8. Angular momentum flux contributions within the cylindrical radial $\mathcal{F}_s/s$ (top) and vertical $\mathcal{F}_z/s$ (bottom) components, which are time integrated over the last 3000 time units and integrated along z over the Northern hemisphere only (because $\mathcal{F}_z$ is antisymmetric about the equator, while $\mathcal{F}_s$ is symmetric). We show MS, MT, RS, MC, and VD contributions. Left: Le $= 6 \times 10^{-5}$ and Pm $= 1$. Right: Le $= 4 \times 10^{-2}$ and Pm $= 1$.

represents the $m = 0$ component of the magnetic (hydrodynamic) contributions to the angular momentum fluxes, whereas the Maxwell (Reynolds) stresses are defined to result from the non-axisymmetric components.

The different flux terms within $\mathcal{F}_s$ and $\mathcal{F}_z$ are each displayed in Fig. 8 for two examples, one with a low and one with a high initial dipolar magnetic field strength. We show results after $z-$integration and time integration over the last 3000 rotation units, when the simulation is approximately in a steady state but with a slowly decaying magnetic field (though at high Lehnert numbers the decay of the magnetic field influences the differential rotation strength substantially). When Le is low (left panels), strong Reynolds stresses in $\mathcal{F}_s$ (especially near the poles) generate differential rotation until they can be nearly perfectly compensated by VD (with opposite signs), with negligible contributions from MC, MS, and MT. This is similar to what we expect from purely hydrodynamical simulations when the zonal flow reaches a steady state (see also appendix A in Astoul & Barker 2023), where RSs from tidal waves balance VD. The MC $\widehat{u_z} \widehat{u_\varphi}$, which represents the large-scale correlations of vertical and azimuthal axisymmetric components, plays a more important role near the poles for $\mathcal{F}_z$ than it does for $\mathcal{F}_s$. This suggests large-scale recirculations in the polar columnar flow, both up and down (because of the opposite signs), from the reflection of the shear layers at the rotation axis. RSs are also important for $\mathcal{F}_z$ and peak

in the outer tangent cylinder (OTC) at locations where the shear layers reflect at the inner/outer boundaries or at the equator. Note that $\mathcal{F}_z$ is antisymmetric about the equator (while $\mathcal{F}_s$ is symmetric), so performing z-integration over the two hemispheres would almost cancel out this component.

When the initial Lehnert number is high (right panels), VD and MC are much less important than in the previous case, and RSs are now balanced by MT. These inhibit development of zonal flows and result in much weaker differential rotation. Interestingly, MS (involving correlations of non-axisymmetric components) are small compared to MT here, which is the opposite of what has been found in Brun (2004) and Browning (2008) in their convective dynamo simulations where MS seem to cancel out differential rotation in some regimes. Stronger MT may partly explain why, for Le $\gtrsim$ Le$_c$, tidally driven zonal flows have more difficulty developing or are completely inhibited from the start for the highest initial Lehnert numbers. Concomitantly, we also observe periodic oscillations on long periods ~ 1500 (or somewhat shorter) in E_{dr}, M_t, and $M_p(m = 2)$, early in the simulations (see the right panels of Figs 2, 3, and 7). These oscillations may correspond with torsional Alfvén waves, restored by the magnetic tension component of the Lorentz force (e.g. the review of Hori et al. 2023). To illustrate the emergence of these waves, we compute the vertically and azimuthally averaged azimuthal velocity inside the shell, such that:
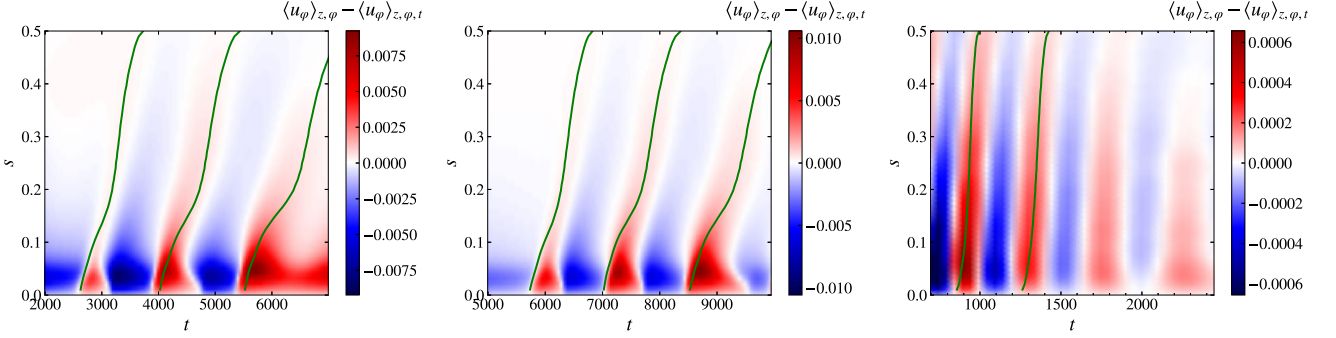
Figure 9. Amplitude of the fluctuating z- and φ-averaged zonal flow $\langle u_\varphi \rangle_{z,\varphi} - \langle u_\varphi \rangle_{z,\varphi,t}$ versus time t and cylindrical radius s for three simulations possibly exhibiting propagating torsional Alfvén waves. The time average for the zonal flow $\langle u_\varphi \rangle_{z,\varphi,t}$ is performed over the whole time range shown in each plot where the oscillations are observed. The green curve shows the Alfvén time-scale t_A (averaged over an approximate cycle around which t_A is drawn) versus s. Left: Le $= 6 \times 10^{-3}$. Middle: Le $= 10^{-2}$. Right: Le $= 2 \times 10^{-2}$.

$$\langle u_\varphi \rangle_{\varphi,z} = \frac{1}{h} \int_{z_i}^{z_o} \langle u_\varphi \rangle_\varphi \, dz, \tag{15}$$

from which we remove the mean background state $\langle u_\varphi \rangle_{z,\varphi,t} = 1/\tau \int^\tau \langle u_\varphi \rangle_{z,\varphi} \, dt$ over an arbitrary time τ (chosen to define a representative mean state) in the manner of Teed, Jones & Tobias (2014). We define $h = (z_o - z_i)/2$, $z_o = \sqrt{1 - s^2}$, and $z_i = \sqrt{\alpha^2 - s^2}$ in the inner tangent cylinder (ITC), and $z_i = 0$ in the OTC. The Alfvén time,[10] which describes the time-scale for radial propagation of these waves over a distance s, is defined by:

$$t_A = \frac{s}{\text{Le} \sqrt{\langle B_s^2 \rangle_{\varphi,z,t}}}, \tag{16}$$

with $B_s = B_r \sin\theta + B_\theta \cos\theta$, the cylindrical component of the magnetic field. The temporally fluctuating mean zonal flows are shown versus s in Fig. 9 for three simulations with increasing initial Lehnert numbers that possibly exhibit torsional waves. The fluctuations of the zonal flows as a function of s and t are nicely explained by the variation of the Alfvén time-scale inside the ITC (equation 16), bending towards higher s and t, when averaging over one cycle around different initial times. This suggests that the oscillatory and wave-like nature of the zonal flows in these simulations is likely to result from the propagation of torsional Alfvén waves. These appear to be excited near the polar regions and to subsequently propagate outwards where they are primarily dissipated, rather than being reflected to form torsional (standing-mode) oscillations.

We observe that the zonal flow oscillation cycle is longer for lower initial Lehnert numbers, for example when comparing the time-scale of the first oscillation for Le $= 6 \times 10^{-3}$ (about 1000 rotation units) and Le $= 2 \times 10^{-2}$ (about 400). It also increases with time in each panel since the poloidal magnetic field, therefore B_s, decreases due to Ohmic diffusion (for instance, it is about 1500 for the second cycle for Le $= 6 \times 10^{-3}$). For Le $= 10^{-2}$, similar time-scales are found as for Le $= 6 \times 10^{-3}$, since torsional oscillations are triggered later in the simulations (see the right panel in Fig. 3), so Le$_p$ (and so B_s) are of the same amplitude as can be seen in Fig. 7 (top panel). It is interesting to see that for Le $= 10^{-2}$ (and for Le $= 6 \times 10^{-3}$), the amplitude of the MT, VD, and MC vary with the sign of the fluctuating zonal flows $\langle u_\varphi \rangle_{z,\varphi} - \langle u_\varphi \rangle_{z,\varphi,t}$, which we illustrate in Fig. B2: when $\langle u_\varphi \rangle_{z,\varphi} < \langle u_\varphi \rangle_{z,\varphi,t}$ (left panels) MT dominate, while

when $\langle u_\varphi \rangle_{z,\varphi} > \langle u_\varphi \rangle_{z,\varphi,t}$ (right panels) VD in $\mathcal{F}_s$ and MC in $\mathcal{F}_z$ take over close to the pole. It is not clear whether the fast oscillations for Le $= 2 \times 10^{-2}$ are of the same nature since this cyclic trend is not observed and MT dominate for all times like in Fig. 8 (right panels). The transition between regimes where zonal flows are strong, like in hydrodynamical cases, or are substantially quenched by MT (which also corresponds with when slow torsional oscillations are observed) can be further interpreted by introducing the backreaction time-scale t_{ap} of the magnetic tension on differential rotation. We define this in a similar way (but modified) as Aurière et al. (2007) and Jouve et al. (2015), as $t_{ap} = l_\Omega/v_{ap}$, with $v_{ap} = \sqrt{\langle B_s^2 \rangle_{\varphi,z}}$ the torsional Alfvén velocity of the magnetic field in the cylindrical direction, and l_Ω is once again the length-scale of variation of the differential rotation.

For Le $< 10^{-3}$, the backreaction time-scale is long compared to both the winding-up time-scale and the Ohmic damping time-scale of Alfvén waves t_η, namely $t_{ap} \gg t_\Omega$ and $t_{ap} \gg t_\eta$, respectively. This means that differential rotation has time to stretch poloidal magnetic field lines to create a strong toroidal component, while Alfvén waves have insufficient time to propagate before being damped by Ohmic diffusion. When Le $\approx$ Le$_c$, we measure (at $t = 100$) $t_{ap} \simeq t_\Omega \simeq t_\eta$ (all taking values around 500). From Fig. 3 (left panel), we indeed note the slight perturbation of E_{dr} to set in at early times for this transitional Lehnert number. For higher initial Lehnert numbers Le $>$ Le$_c$, t_{ap} is smaller at a fixed time while t_Ω and t_η both stay the same, so that $t_{ap} \ll t_\Omega$ and $t_{ap} \ll t_\eta$. This means that Alfvén waves have time to propagate before being damped and their large-scale axisymmetric correlations (MT) can act on differential rotation to quench it.

3.3 Tidal dissipation rates as a function of Le

The variation in the strength of differential rotation (with Le and time) has a substantial impact on tidal viscous dissipation rates D_v, as we show in the bottom panel of Fig. 7. For low poloidal Lehnert numbers Le$_p$, since E_{dr} is very close to the hydrodynamical prediction (in the upper panel), D_v also matches the prediction computed with hydrodynamic (Le $= 0$) non-linear simulations (presented in AB22) when the simulation reaches a time-averaged steady state.

On the other hand, for much higher initial Lehnert numbers Le $>$ Le$_c$, D_v ends up much closer to the linear hydrodynamical prediction, since differential rotation is too weak to impact viscous dissipation in these simulations. Thus, for our set of parameters, the main ingredient controlling the magnitude of viscous dissipation is the strengths of the zonal flows, with the magnetic fields themselves playing only an indirect role on D_v. For Pm $= 1$, the Ohmic

---

[10]Since B_s is antisymmetric compared to the equator, the square of it has been taken before performing the z average.
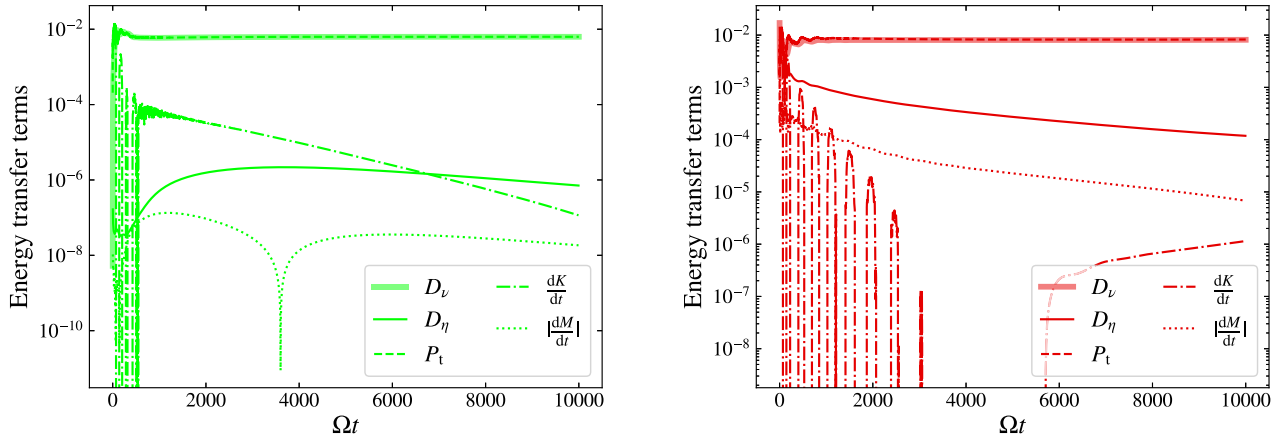
Figure 10. Time evolution of contributions to evolution of the total energy in equation (7). We show, in order, viscous dissipation, Ohmic dissipation, tidal power, and time derivative of the kinetic and magnetic energies (Pm = 1). We omit the Poynting flux, since it is found to be negligibly small in both panels. The energy equation is thus accurately satisfied in our simulations. Left: Le = 6×10^{-5} (weak field). Right: Le = 2×10^{-2} (strong field).

dissipation D_η is quite low in all simulations compared to the tidal power and viscous dissipation, which mainly balance each other, as is shown in Fig. 10 for two different initial Lehnert numbers. In these simulations, the energy balance is well satisfied with an error at the end of the simulation of one-tenth of a percent for Le = 2×10^{-2} (and much lower for 6×10^{-5}), which could be reduced even further by increasing the spatial (and temporal) resolution.

For large Lehnert numbers, the values of the dissipation rates D_η and D_ν are quite different from what is predicted by linear MHD models with an imposed dipolar magnetic field only (dotted black lines in Fig. 7, and Lin & Ogilvie 2018). Indeed, linear viscous dissipation is predicted to be strongly affected by the presence of a magnetic field (with clear peaks and troughs) for Le $\gtrsim$ Le$_c$, while linear Ohmic dissipation is expected to be dominant. However, these linear predictions for D_ν and D_η do not account for toroidal and non-axisymmetric components of the magnetic field, the modest differential rotation that is present, and the fact the initial dipole decays over time, which explains why D_η drops over time in Fig. 10, leaving D_ν as the only dominant sink of energy injected by tidal power. Early time values of D_ν and D_η in non-linear simulations may be closer to linear MHD predictions, but it is difficult to be definite because the time to reach steady state is almost always comparable with (or longer than) the Ohmic decay time for the imposed field.

4 DEPENDENCE ON THE MAGNETIC PRANDTL NUMBER

### 4.1 Trends varying the magnetic Prandtl number

We have also performed simulations varying the initial Lehnert number with different magnetic Prandtl numbers Pm $\in [10^{-1}, 2, 5]$ (for the same Ek) to explore the impact of variations in the Ohmic diffusivity (relative to the viscosity). The energy in the differential rotation E_{dr} and the viscous dissipation D_ν versus Le$_p$ are displayed in Fig. 11, with linear and non-linear hydrodynamical predictions (in black dashed dotted and solid lines, respectively) as in Fig. 7 for Pm = 1. Similarly, we also plot linear MHD predictions (in black dotted lines) with an imposed dipolar magnetic field with a strength given by the initial Le$_p$ (following Lin & Ogilvie 2018). As for Pm = 1 (Fig. 7), this exhibits a complicated dependence on Le$_p$ for each Pm. These predictions do not clearly match our simulations for larger Le (where they differ from hydrodynamical predictions),

probably because the field in them has substantial toroidal and non-axisymmetric components, and more importantly because the initial dipole decays, unlike what is assumed in the linear calculations used to compute the black dotted lines. In Fig. 12, we compute linear MHD values (for a fixed background dipolar field) of the viscous and Ohmic dissipations for the Lehnert and magnetic Prandtl numbers investigated here. For high magnetic Prandtl numbers Pm = 2 and 5, it is interesting to see that viscous dissipation always dominates Ohmic dissipation over Le. It differs from what has been found in Lin & Ogilvie (2018, fig. 4) for Pm $\ll$ 1, where D_η takes over D_ν for Le $\gtrsim 10^{-4}$. For Pm = 1, D_η starts to be dominant for Le $\gtrsim 2 \times 10^{-2}$ (in Fig. 12), which may explain why the non-linear viscous dissipation in Fig. 7 starts to be seriously mitigated at this high Lehnert number. Lastly, for Pm = 0.1, $D_\eta \gtrsim D_\nu$ from Le $\gtrsim 8 \times 10^{-3}$ (in Fig. 12), and the surge (and drops) in non-linear D_ν in Fig. 11 (right-bottom panel) around Le = 10^{-2}, may correspond to the highest peak (and drops) found in Fig. 12. However, although Ohmic dissipation dominates for lower Pm, Ohmic decay is even faster for this low magnetic Prandtl number, making a direct comparison between linear and non-linear MHD predictions even more difficult.

For higher magnetic Prandtl numbers, two regimes, either having strong (for small Le$_p$) or weak (for larger Le$_p$) differential rotation, are observed in a similar way as for Pm = 1. Unlike cases with Pm = 1, oscillations at the transition for Pm = 2 (e.g. when Le = 2×10^{-3} or 6×10^{-3}) are associated with repeated brief surges of the total poloidal magnetic energy M_p, concomitantly with an increase in M_t, but after E_{dr} peaks. This is shown in Fig. 13. In these simulations, the quadrupolar component in the poloidal magnetic field (created by stretching of the axisymmetric toroidal magnetic field by tidal waves) may play a role in the cyclic mitigation of differential rotation, as evidenced in Fig. 14. Indeed, unlike in the previous cases when Pm = 1, we notice the importance of MS (at the first 'trough' in E_{dr}) which reflect here the strength of non-axisymmetric magnetic correlations. For low Le, we also note the important role of the zonal flows, which more strongly shape magnetic fields for high magnetic Prandtl numbers, and in particular poloidal magnetic field lines, as we can see in Fig. 1 (bottom-middle panel).

For an even larger magnetic Prandtl number Pm = 5, we also observe the transition between the two regimes, but it is shifted further towards a lower Lehnert number Le$_c \approx 10^{-3}$, while it was Le$_c \approx 2 \times 10^{-3}$ for Pm = 2, and Le$_c \approx 3 \times 10^{-3}$ for Pm = 1.
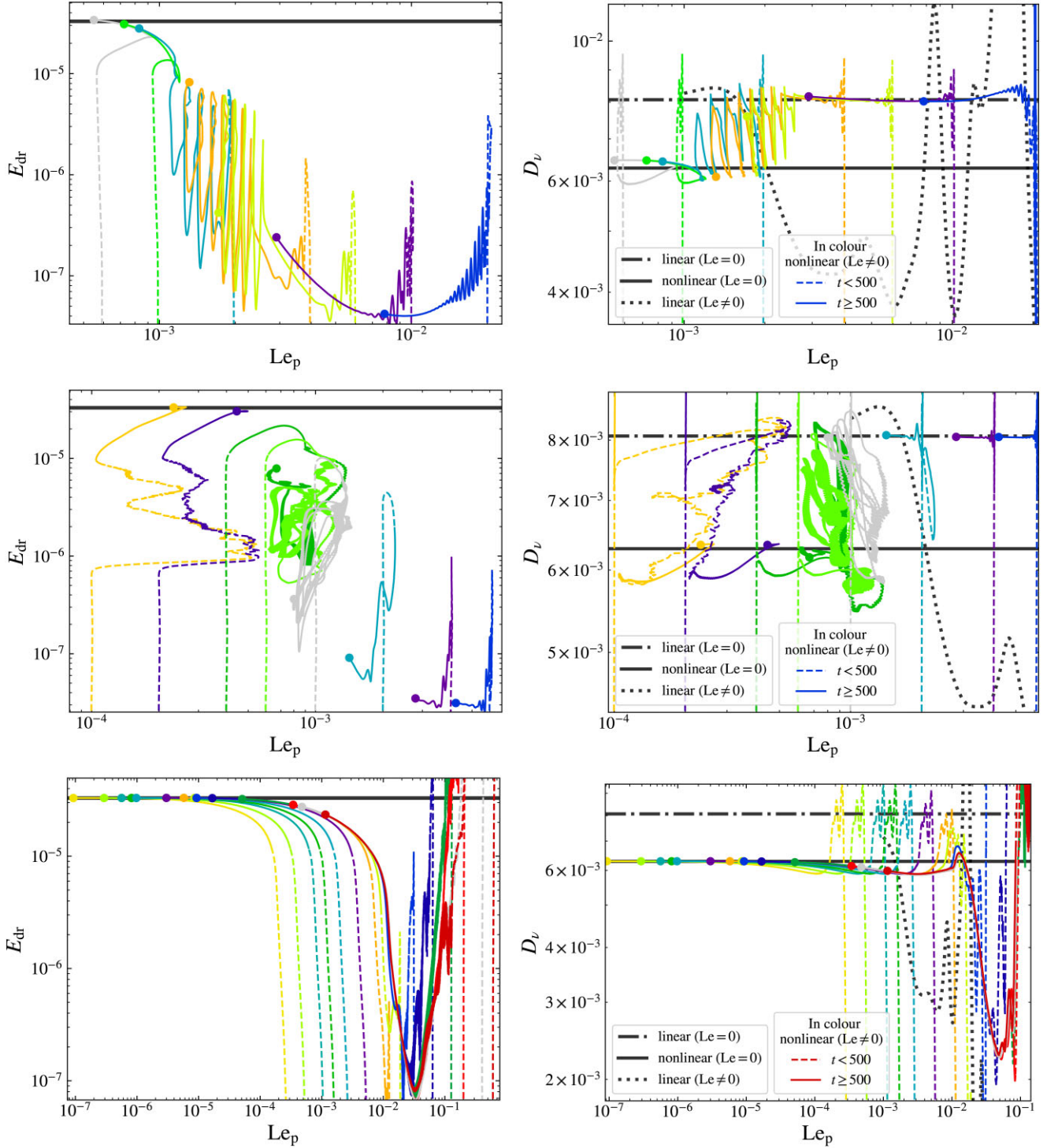
Figure 11. Same as Fig. 7, but for Pm = 2 (top, simulations ran until $t = 20\,000$ here), Pm = 5 (middle), and Pm = 0.1 (bottom).

With increasing Pm, the magnetic Ekman number (Em = Ek/Pm) decreases, and so does D_η, with the latter always being negligible compared to P_t and D_ν. We do not observe a clear transition for a low magnetic Prandtl number Pm = 0.1, though it may arise around Le $\approx 10^{-2}$. In these simulations, the Ohmic dissipation D_η is non-negligible at early times, while D_ν is smaller. However, since Ohmic diffusivity Em = $10^{-4} >$ Ek is important there, magnetic fields decay relatively rapidly, and so does D_η. The non-linear

hydrodynamical regime is then reached more rapidly for Pm = 0.1 as Le$_p$ more rapidly decays with time in this case.

The heuristic scaling law derived in Lin & Ogilvie (2018, hereafter LO18) to distinguish between linear regimes dominated by (approximately hydrodynamic) inertial or (inherently magnetic) Alfvén waves may be applied and modified for our study. When Pm $\ll 1$, they found that inertial waves prevail as long as Le $< \mathcal{O}(\text{Em}^{2/3})$, with a prefactor depending on the direction of the magnetic field compared
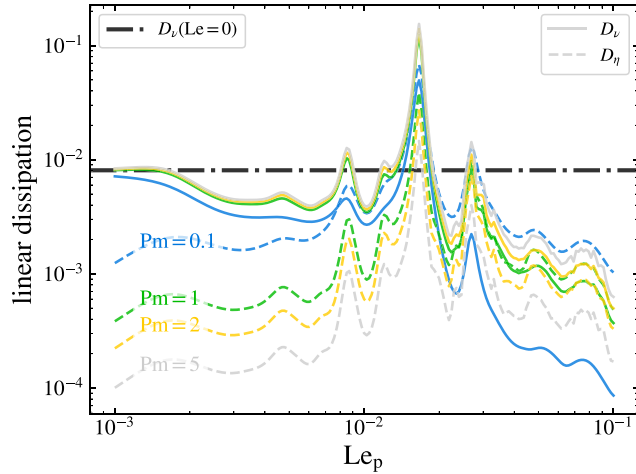
Figure 12. Viscous and Ohmic dissipation D_η and D_ν computed in linear MHD calculations with a fixed background dipolar magnetic field as in Lin & Ogilvie (2018), versus dipolar Lehnert number $\mathrm{Le_p}$ for various magnetic Prandtl numbers Pm. Viscous dissipation from a linear hydrodynamical calculation has been put for reference in black.

to that of the (wave) shear layer of width l (and of the zonal flow here, which modifies the direction of wave propagation). The inertial wave propagation time and the time-scale for setting up the zonal flow are constrained by either Ohmic diffusivity or viscosity, according to the value of Pm. For $\mathrm{Pm} \gg 1$, the viscous damping time-scale l^2/Ek should be preferred compared to the Ohmic diffusion one. In the intermediate regime when $\mathrm{Pm} \sim 1$, a geometric mean diffusion time could be used instead, such that the diffusion time-scale across a wave beam becomes $\tau_i = l^2/\sqrt{\mathrm{EkEm}}$ instead. Using the same heuristic arguments as in LO18 with the above time-scale, LO18's scaling law becomes $\mathrm{Le} = \mathcal{O}(\mathrm{Ek}^{2/3}/\mathrm{Pm}^{1/3}) = \mathcal{O}(\mathrm{Em}^{2/3}\mathrm{Pm}^{1/3})$. It is reported in Table 2 for Ek and Pm used in our simulations, along with the values of $\mathrm{Le_c}$ roughly estimated from Figs 7 and 11. For $\mathrm{Pm} \geq 1$, the scaling law may be relevant to predict the transition with an overall proportionality constant of approximately 5, though it is less clear that it holds for $\mathrm{Pm} = 0.1$. Such a proportionality constant could be related to the fact that the inertial wave shear layers are inclined with respect to the magnetic field lines (close to the pole it is about $\theta = \arcsin(\omega/m)$ from the rotation axis because the poloidal field is nearly vertical). Further simulations exploring a wider range of parameters, particularly varying Ek as well as Pm, would be useful to explore the validity of this trend before we can confidently extrapolate it to stars and planets. Nevertheless, the values here for $\mathrm{Le_c}$ in our simulations are close to (or within) the ranges of values expected in stars and hot Jupiters, as discussed in Section 2.1. Thus, we may expect complex interactions between tidal flows and magnetic fields in many stars and planets.

4.2 Identification and analysis of magnetohydrodynamic instabilities

In our simulations with $\mathrm{Pm} = 5$ and $\mathrm{Le} \sim \mathrm{Le_c}$ (which have both moderately strong differential rotation and magnetic field), we have observed MHD instabilities to operate, particularly for[11] $\mathrm{Le} \in [4 \times 10^{-4}, 10^{-3}]$. In Fig. 15, we show snapshots of the meridional plane

in two examples exhibiting possible MHD instabilities. These show growth of localized spatially oscillatory patterns in the magnetic field close to the poles where the differential rotation is strongest, as seen in both the axisymmetric ($\langle B_\theta \rangle_\varphi$) and non-axisymmetric ($B_\varphi^{\mathrm{naxi}} = B_\varphi - \langle B_\varphi \rangle_\varphi$) components (each chosen to most clearly visualize the instability). These snapshots have been taken at times which correspond to a maximum of the poloidal magnetic energy, as we can see in Fig. 16. This time is also correlated with abrupt changes in the toroidal magnetic energy and differential rotation. For $\mathrm{Le} = 4 \times 10^{-4}$ (left panel) the rapid, approximately exponential, growth of the poloidal magnetic energy is associated with a strong decrease of E_{dr} (and to a lesser extent M_t) around $t = 4800$, while for $\mathrm{Le} = 10^{-3}$ (right panel), we note periodic quasi-simultaneous bursty behaviours in each of M_p, M_t, and E_{dr} (and E_{dr} slightly precedes the two others). These periodic bursts are associated with sinks of the viscous dissipation D_ν and tidal power P_t, which drop by approximately $20 - 30$ per cent during these periods. The periods of exponential growth in magnetic energy, and the fall in E_{dr}, indicate the likely onset of MHD instabilities driven by the differential rotation. We have measured growth rates γ during the exponential growth phases of different magnetic components, which we present in Table 3.

For $\mathrm{Le} = 4 \times 10^{-4}$, the surge (drop) of M_p (E_{dr} and M_t), seems to be concomitant with a strong increase of the $m = 1$ toroidal component, and to a lesser extent, to the rise of the $m = 2$ components, as shown in Fig. 16. These modes (along with the $m = 3$ mode to a lesser degree, not shown here) are excited at the forcing frequency $\omega = 1.1$, which precludes possible triadic resonances and parametric instabilities as found in AB22. For $\mathrm{Le} = 10^{-3}$, the $m = 1$ mode does not seem to trigger the initial instability associated with the bursty behaviour of the magnetic field, but may rather be a consequence of it, since it arises later in the simulation. Before the $m = 1$ mode kicks in, a second sharper slope is visible in $M_p(m = 2)$ and $M_t(m = 2)$ peaks, but it is not present in the axisymmetric poloidal magnetic energy $M_p(m = 0)$, so both $m = 0$ and $m \neq 0$ (first linked to $m = 2$ and then to $m = 1$ modes) instabilities could be in operation. Thus, it is difficult to determine from these time-series alone which magnetic components (axisymmetric or non-axisymmetric) induce the other – i.e. whether the instability is axisymmetric or non-axisymmetric (or both), and which component could be a consequence of the other. It should be noted than higher growth rates are estimated for non-axisymmetric $m = 2$ (and $m = 1$) magnetic energy components in both simulations. Lastly, an important contribution of the (non-axisymmetric) radial MS stands out close to the pole when the instability is triggered for $\mathrm{Le} = 4 \times 10^{-4}$ (see Fig. 17). These strong MS, that are also present for $\mathrm{Le} = 10^{-3}$, have been observed, to a lesser extent, in some simulations for $\mathrm{Pm} = 2$ (see Fig. 14). They seem to partially balance the RS generating the differential rotation, thereby requiring somewhat weaker VD to maintain the zonal flow.

Without any magnetic fields, the tidally driven zonal flow for $\omega = 1.1$ is hydrodynamically stable according to the Rayleigh criterion[12] (see AB22). However, since the angular velocity decreases outwards radially from the pole to the equator in our simulations, the cylindrical zonal flow could host magnetorotational instabilities (MRI) in the presence of magnetic fields (see e.g. Balbus &

---

[11] In these simulations, we increased the spatial resolution to guarantee that the instabilities observed are well resolved, with a maximum number of

Chebyshev radial nodes of $n_{r,\,\mathrm{max}} = 161$, and maximum degree and order of the Legendre polynomials $l_{\mathrm{max}} = 341$ and $m_{\mathrm{max}} = 50$.

[12] This states that rotating flows in which angular momentum does not decrease outwards from the axis are hydrodynamically stable to axisymmetric instabilities.
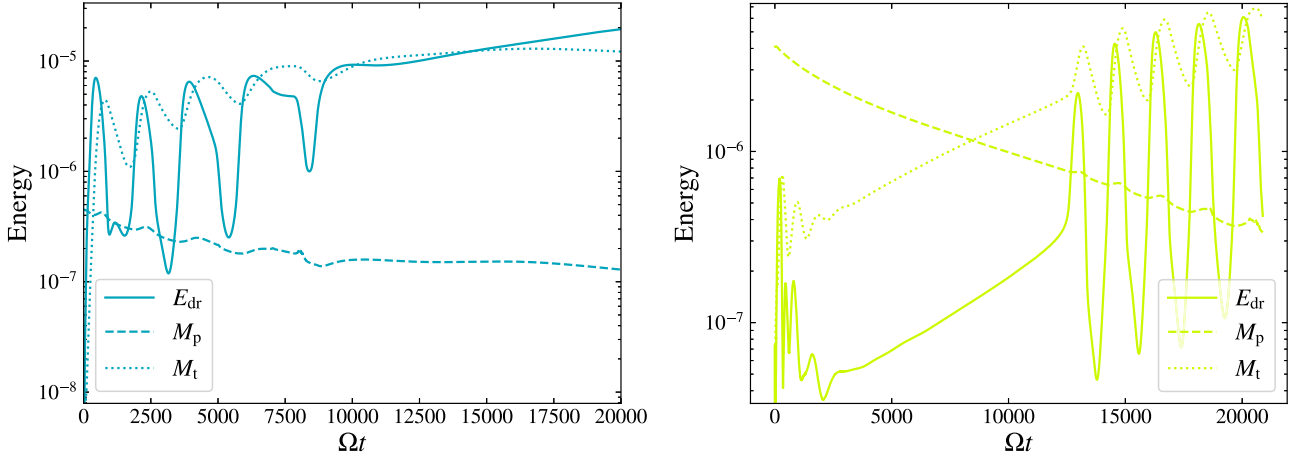
Figure 13. Poloidal M_p and toroidal M_t magnetic energies along with energy in differential rotation E_{dr} versus time for two simulations with Pm = 2 and Le = 2×10^{-3} (left) and Le = 6×10^{-3} (right).
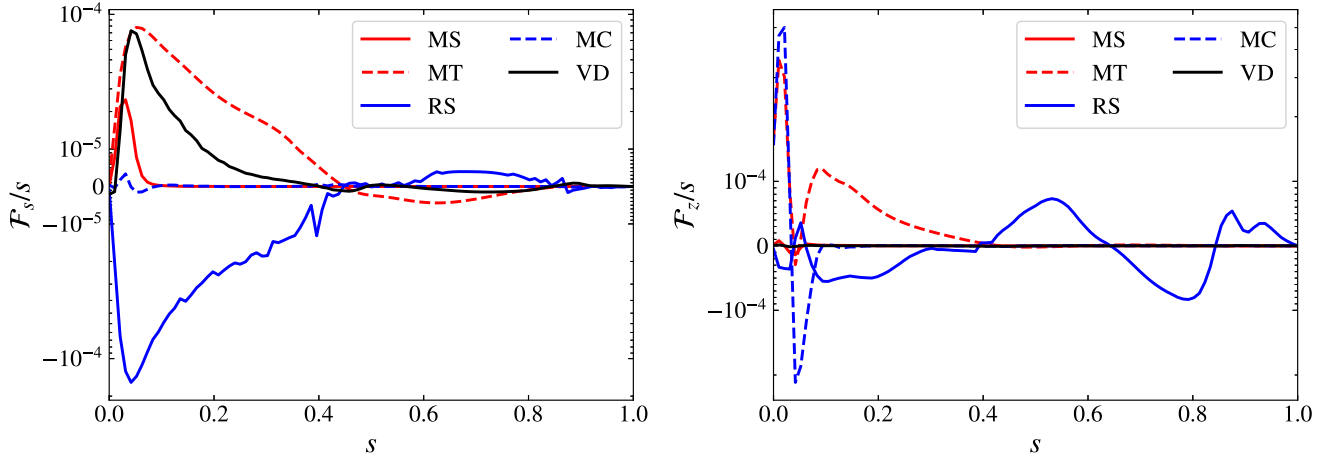
Figure 14. Flux terms within the cylindrical $\mathcal{F}_s/s$ (left) and vertical $\mathcal{F}_z/s$ (right) angular momentum fluxes, integrated along z over the Northern hemisphere only, for Le = 2×10^{-3} and Pm = 2 at $t = 650$.

Table 2. Transitional Lehnert numbers Le_c for various magnetic Prandtl numbers Pm, estimated from the scaling law or approximatively inferred from Figs 7 and 11.

Le_c \ Pm	0.1	1	2	5
$\mathcal{O}(Em^{2/3}Pm^{1/3})$	$\mathcal{O}(10^{-3})$	$\mathcal{O}(5 \times 10^{-4})$	$\mathcal{O}(4 \times 10^{-4})$	$\mathcal{O}(3 \times 10^{-4})$
Inferred	$\gtrsim 10^{-2}$	3×10^{-3}	2×10^{-3}	10^{-3}

Hawley 1998; Balbus 2009, for an introduction). These instabilities have been widely studied, for example in the context of accretion discs, for their capacity to transport angular momentum outwards through turbulence (e.g. Balbus & Hawley 1991; Ogilvie & Pringle 1996), or in the context of the geodynamo (e.g. Acheson 1983; Petitdemange, Dormy & Balbus 2013). Local analytical models have been developed to study both axisymmetric and non-axisymmetric MRI with different topologies of the magnetic field (e.g. Acheson & Gibbons 1978; Balbus & Hawley 1991; Kirillov & Stefani 2010, and many others). The instability of an axial (vertical) magnetic field in a cylindrical Taylor–Couette flow was initiated by Velikhov (1959), but its importance was realized when it was rediscovered by

Balbus & Hawley (1991), and it is now known as the standard MRI (SMRI). The axisymmetric instability occurring with a combination of an axial and azimuthal magnetic fields is now sometimes called the helical MRI (HMRI; e.g. Hollerbach & Rüdiger 2005; Kirillov & Stefani 2010, where the latter points out its relation to SMRI), and the non-axisymmetric instability of a purely azimuthal magnetic field is called the azimuthal MRI (AMRI; e.g. Acheson & Gibbons 1978; Rüdiger et al. 2007; Hollerbach, Teeluck & Rüdiger 2010; Guseva et al. 2017).

In Appendix C1, we have explored the possible roles of axisymmetric SMRI or HMRI to explain the instability observed close to the poles that varies along the rotation axis, based on applying the local linear stability analysis of Kirillov & Stefani (2010). The growth rate of the most unstable mode has been calculated by solving the resulting quartic dispersion relation. Predicted growth rates match relatively well those measured in our simulations (see Fig. B3, Table 3, and Table C1), but the predicted vertical wavenumbers are typically lower than the measured ones.

Nevertheless, there are difficulties in applying the local analysis, partly because we must adopt appropriate values of the parameters
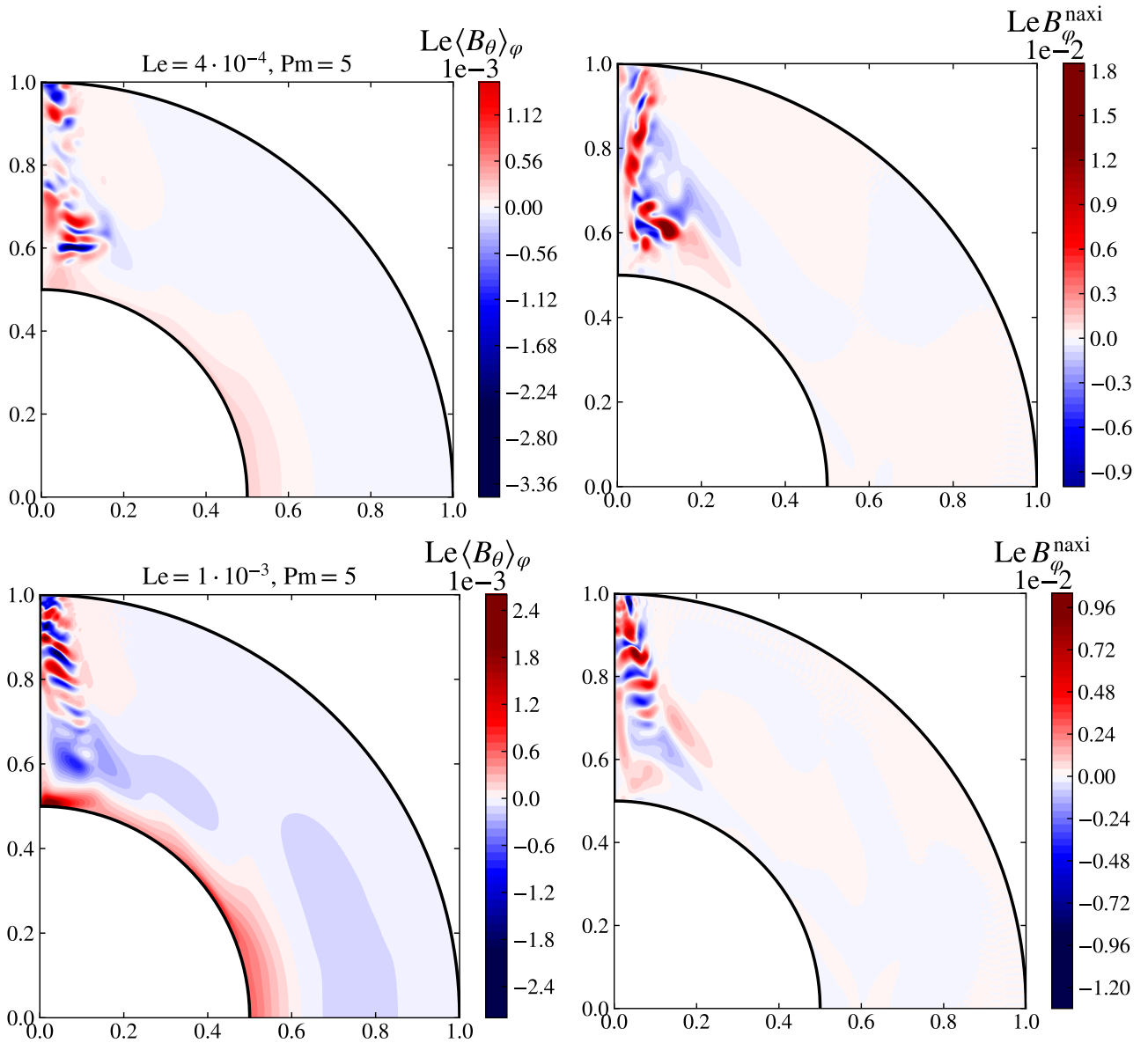
Figure 15. Axisymmetric (left) and non-axisymmetric (right) latitudinal and azimuthal magnetic fields (Le$\langle B_\theta \rangle_\varphi$ and Le$B_\varphi^{\mathrm{naxi}}$, respectively) for two simulations exhibiting instabilities near the poles. These cases have Le $= 4 \times 10^{-4}$ at $t = 4850$ (top) and Le $= 10^{-3}$ at $t = 2950$ (bottom), both with Pm $= 5$.

used in the model to compare with simulations, such as the vertical and azimuthal magnetic field strengths, and the shear rate, which we have estimated from the simulations. These vary substantially as a function of position, even within the region where the instability is observed, and with time. In addition, the short-wavelength (WKBJ[13]) approximations used to derive the dispersion relation may not be fully satisfied, as we discuss further in the appendix. Finally, the basic state is evolving in time (i.e. specifically the differential rotation and magnetic field profiles), whereas the local WKBJ theory assumes a static or slowly varying (compared to the growth time of the mode) basic state.

In the two simulations examined in this section, the axisymmetric azimuthal magnetic field is strongly dominant (see Fig. 16). Therefore, and as discussed earlier, non-axisymmetric perturbations driven

by this field may also be excited (see e.g. Hollerbach et al. 2010; Kirillov & Stefani 2010). We have thus also explored the possibility of non-axisymmetric AMRI in Appendix C2 following Acheson & Gibbons (1978) and Meduri, Lignières & Jouve (2019). Although the same limitations apply to this model as for SMRI/HMRI, the analytically predicted growth rates could also be consistent with the measured ones (see Fig. C1), both for $m = 1$ or 2 non-axisymmetric perturbations.

In conclusion, both HMRI and non-axisymmetric AMRI could predict MHD instabilities observed in the polar regions of these simulations, as summarized in Fig. 18, where the growth rate γ is higher in some regions (especially for AMRI) but overall compatible with the measured values in Table 3, and with (radial) magnetic perturbations shown in black contours (similarly as fig. 10 of Jouve, Lignières & Gaurat 2020). To apply these local stability analyses and compute γ, azimuthal averages of the rotation and shear rates,

---

[13]Wentzel–Kramers–Brillouin-Jeffrey
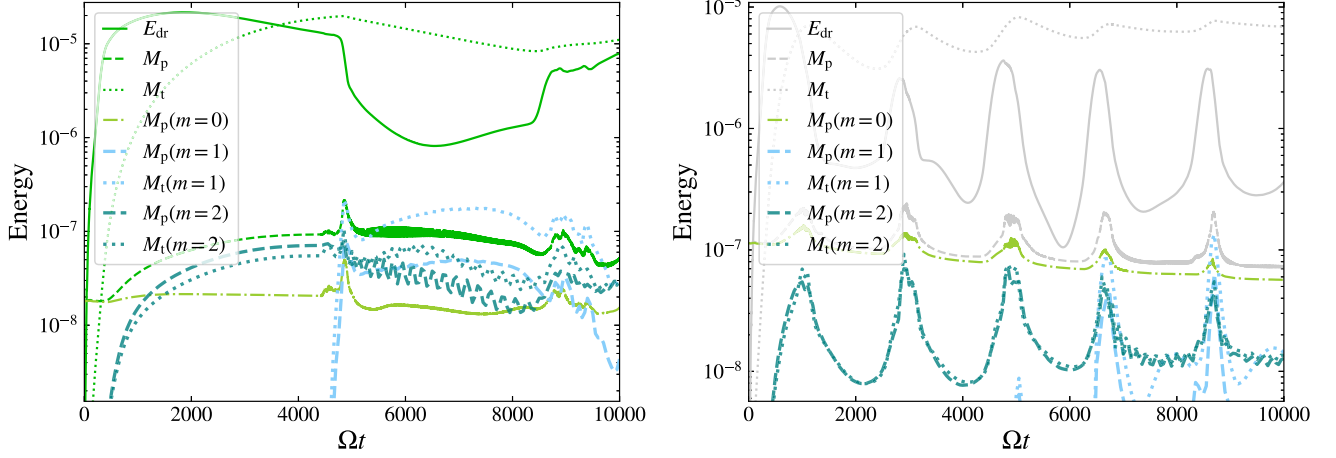
Figure 16. Evolution of various key energy terms (see the legends) in two simulations when Pm = 5. Left: Le = 4×10^{-4}. Right: Le = 10^{-3}.

Table 3. Measured growth rates of the (non-)axisymmetric poloidal and toroidal magnetic energies assuming that $M_{p,t} \propto \exp(2\gamma t)$ at the burst and performing a linear interpolation. (1) and (2) refers to the first and second slopes, before and after $t = 2800$, respectively.

Le	$\gamma(M_p)$	$\gamma\left(M_p^{m=0}\right)$	$\gamma\left(M_p^{m\neq0}\right)$	$\gamma\left(M_t^{m\neq0}\right)$
4×10^{-4}	6.5×10^{-3}	4.7×10^{-3}	7.1×10^{-3}	8.3×10^{-3}
10^{-3} (1)	7.1×10^{-4}	5.1×10^{-4}	1.7×10^{-3}	2.5×10^{-3}
10^{-3} (2)	3.4×10^{-3}	/	1.2×10^{-2}	10^{-2}

vertical and azimuthal magnetic fields, and their gradients, have been computed at each point of the polar regions [equations (C3) and (C5)], and we choose $k_z = 126$ for Le = 4×10^{-4} and $k_z = 94$ for Le = 10^{-3}, along with $k_x = 63$ (see Table C1) based on by-eye fitting.

A more comprehensive local analysis involving non-axisymmetric perturbations with both axisymmetric poloidal and toroidal magnetic fields may be useful to have better predictions of the unstable modes involved in the instabilities seen in the simulations for Le = 4×10^{-4} and 10^{-3}. But any such local analysis is unlikely to substantially improve agreement with simulations, since the basic state is evolving in time, and the modes are not truly local since the basic state varies on a scale not much larger than the wavelengths of the modes (particularly with cylindrical radius). Finally, the non-axisymmetric analysis assumes exponentially growing normal modes, which we show in the appendix is unlikely to be strictly valid due to the effects of the differential rotation. Nevertheless, our analysis has identified the likely origin of the instabilities observed to be (axisymmetric and/or non-axisymmetric) MRI driven by the differential rotation. Broadly similar wavelengths and growth rates can be obtained in these analyses with suitable parameter choices, keeping in mind all of the above caveats. The role of the MRI in controlling tidally driven differential rotation – and its impact on tidal dissipation rates – is therefore worth studying further.

5 CONCLUSIONS

We have explored the interactions of magnetic fields and tidally excited inertial waves in MHD non-linear models of the convective envelopes of stars and gaseous planets. Our goals were to determine the influence of the field on tidal dissipation rates, and hence for the spin–orbit evolution of many astrophysical systems, but also to study the effects of the flow on the magnetic field. We imposed an initial dipolar field (thought to be generated by a convective dynamo) aligned with the rotation axis, with a strength determined by its Lehnert number Le, and explored the non-linear evolution of both the field and the tidal flow using MHD simulations. Our simulations restricted the tidal frequency to one value in the inertial wave range ($\omega = 1.1\Omega_0$, since this case has been well explored hydrodynamically in Ogilvie 2009; Favier et al. 2014, AB22, AB23), considered a deep convective shell with fractional radius 0.5 (relevant for some low-mass stars or giant planets with large stably stratified dilute cores), and fixed the Ekman number to a value approximately consistent with mixing-length expectations for a turbulent viscosity in solar-like stars. The non-linear interactions of tidal waves and magnetic fields have been found to be complex, with several different regimes depending on Le and the magnetic Prandtl number Pm.

For small Le $\lesssim$ Le$_c \ll 1$, below a critical threshold Le$_c$, the tidal waves behave similarly to in hydrodynamical simulations, non-linearly generating differential rotation in the form of zonal flows (strongest near the poles in our simulations). These strong zonal flows effectively stretch the initial dipolar magnetic field to produce an axisymmetric toroidal field via the Ω−effect. Moreover, non-axisymmetric ($m = 2$) wave-like tidal flows also interacts with these axisymmetric magnetic components to create quadrupolar poloidal and toroidal magnetic components. However, these magnetic fields are not observed to noticeably modify tidal dissipation rates over hydrodynamical non-linear simulations, where zonal flows remain strong and produce observable differences with linear hydrodynamical predictions (as in AB22 and AB23).

For stronger fields with Le $\gtrsim$ Le$_c$, tidally generated zonal flows are substantially inhibited, primarily by magnetic torques (from the contributions of axisymmetric components of the field to the total Maxwell stresses[14]) arising from the large-scale poloidal field. For Le $\sim$ Le$_c$, we observe complex interactions involving the excitation of torsional Alfvén waves (outwardly propagating from their launching sites near the poles) leading to oscillations in both the zonal flows and the field with a frequency proportional to the (cylindrical)

---

[14](Total) Maxwell stresses often refers to both axisymmetric (torque) and non-axisymmetric (stress) magnetic contributions that we distinguish in the present study.
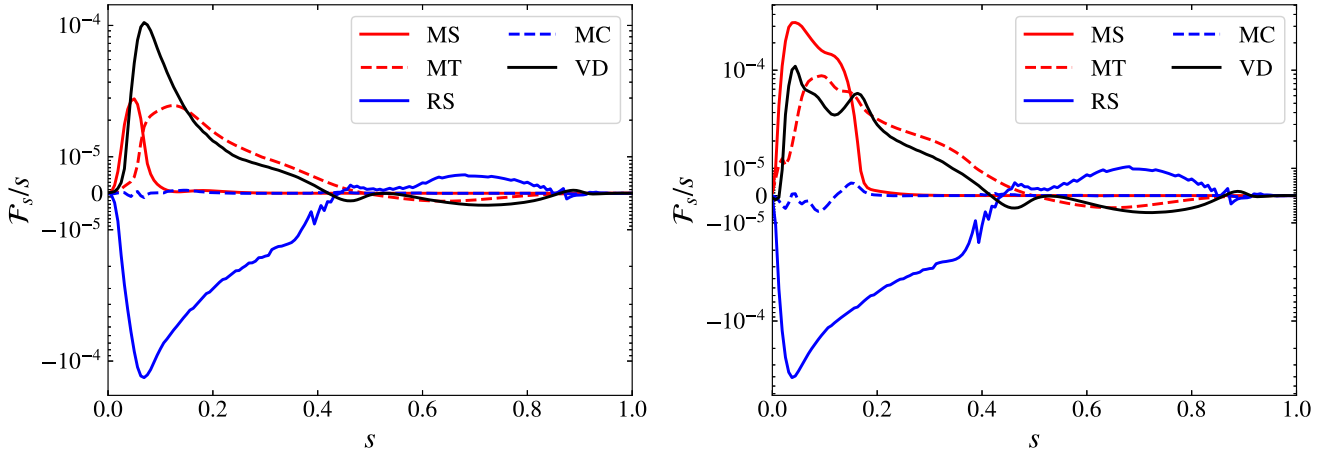
Figure 17. Flux terms within the radial (cylindrical) $\mathcal{F}_s/s$ angular momentum flux integrated along z, for Le $= 4 \times 10^{-4}$ and Pm $= 5$ before and close to the peak of M_p (see Fig. 16) at $t = 4200$ (left) and $t = 4850$ (right), respectively.
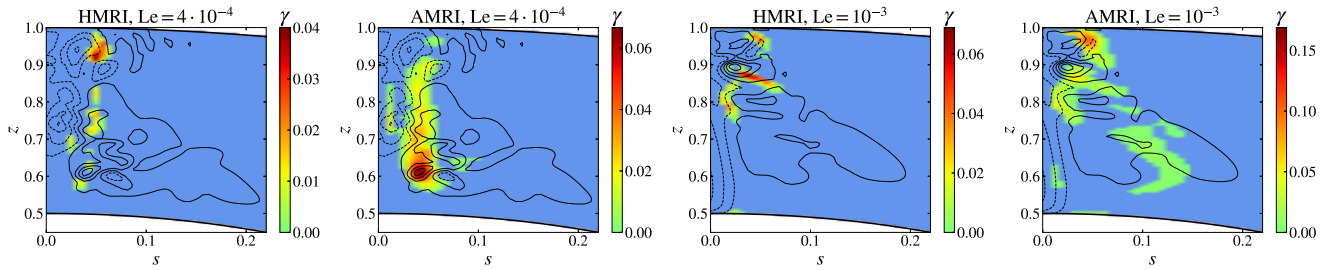
Figure 18. 2D colour maps of the growth rate γ in the polar region for the two simulations with Pm $= 5$ and Le $= 4 \times 10^{-4}$ (the two leftmost panels) and Le $= 10^{-3}$ (the two rightmost panels), from local stability analyses of the axisymmetric helical (HMRI) and non-axisymmetric azimuthal (AMRI) with $m = 1$ (second panel) and $m = 2$ (fourth panel) MRIs. Blue regions (also found everywhere for $s > 0.22$) indicate decaying modes (i.e. with $\gamma < 0$). Black contours represent the radial magnetic field $B_r(\varphi = 0)$.

radial field strength. For smaller Le, their frequency decreases, with magnetic torques becoming weaker, differential rotation becoming stronger, and the Alfvén time-scale becoming longer than the Ohmic diffusion time-scale, leading to a predominantly hydrodynamical regime. For Le $\gtrsim$ Le$_c$, (viscous) tidal dissipation rates transition to a regime where they attain values close to the hydrodynamic linear theoretical predictions without zonal flows (despite the initial field being strong enough to modify linear predictions by itself).

For some simulations with Le $\sim$ Le$_c$, we have identified the MRI to operate, which strongly modifies the differential rotation when it occurs. To verify this interpretation, we have performed local analyses of the axisymmetric MRI in the presence of a poloidal and toroidal field, as well as the (weakly) non-axisymmetric MRI with a toroidal field. Our results suggest that the MRI is likely to be in operation where the differential rotation is strongest in our simulations, with growth rates and axial wavelengths broadly comparable to those observed numerically. In the simulation with Le $= 10^{-3}$ and Pm $= 5$, the MRI produces cyclic, bursty behaviour in the differential rotation and magnetic field, somewhat reminiscent of predator–prey dynamics, while in the simulation with Le $= 4 \times 10^{-4}$, it has the sole effect of strongly mitigating differential rotation.

The transitional Le$_c$ found in our simulations is similar to some estimates of Le near the surfaces, and in PMS phases, of low-mass stars (see Table 1) and in hot Jupiters. This suggests that we might

expect a complex interplay between magnetic fields and tidal flows in stars and planets. This is particularly the case if we interpret our diffusivities as turbulent ones, so that we might expect Pm $= O(1)$ in stars and planets, but less clear if the relevant diffusivities are microscopic ones.

There are many ways in which our study should be extended. First, we should explore a wider range of tidal frequencies, amplitudes, and convective shell thicknesses. In our simulations, the magnetic field led to tidal dissipation rates approaching hydrodynamic linear theoretical predictions, and it is important to explore whether this result is robust and is also found in other cases (including those adopting an imposed 'background magnetic field' instead of an initial imposed field). Introducing convection and performing self-consistent simulations of convective dynamos interacting with tidal flows would be particularly interesting, as well as exploring possible tidally driven dynamos (as done for the elliptical instability in Cébron & Hollerbach 2014; Vidal et al. 2018, in intermediate-mass stars with radiative envelopes). The influence of density stratification within the anelastic approximation, and the roles of an interior radiation zone, are also important to explore in future work.

ACKNOWLEDGEMENTS

DATA AVAILABILITY

The data underlying this article will be shared on reasonable request to the corresponding author.

REFERENCES

Abbassi S., Rieutord M., Rezania V., 2012, MNRAS, 419, 2893

Abramowitz M., Stegun I. A., 1972, Handbook of Mathematical Functions. Dover Publications Inc., New York

Acheson D. J., 1983, Geophys. Astrophys. Fluid Dyn., 27, 123

Acheson D. J., Gibbons M. P., 1978, Phil. Trans. R. Soc. Lond. A, 289, 459

Anufriev A. P., Jones C. A., Soward A. M., 2005, Phys. Earth Planet. Inter., 152, 163

Astoul A., Barker A. J., 2022, MNRAS, 516, 2913

Astoul A., Barker A. J., 2023, ApJ, 955, L23

Astoul A., Mathis S., Baruteau C., Gallet F., Strugarek A., Augustson K. C., Brun A. S., Bolmont E., 2019, A&A, 631, A111

Aubert J., 2018, Geophysi. J. Int., 214, 531

Aurière M. et al., 2007, A&A, 475, 1053

Balbus S., 2009, Scholarpedia, 4, 2409

Balbus S. A., Hawley J. F., 1991, ApJ, 376, 214

Balbus S. A., Hawley J. F., 1998, Rev. Mod. Phys., 70, 1

Barker A. J., 2020, MNRAS, 498, 2270

Barker A. J., 2022, ApJ, 927, L36

Bekki Y., Cameron R. H., Gizon L., 2022, A&A, 662, A16

Bolmont E., Mathis S., 2016, Celest. Mech. Dyn. Astron., 126, 275

Braginskiy S. I., 1970, Geomag. Aeron., 10, 1

Browning M. K., 2008, ApJ, 676, 1262

Brun A. S., 2004, Sol. Phys., 220, 333

Brun A. S., Browning M. K., 2017, Living Rev. Solar Phys., 14, 4

Cébron D., Hollerbach R., 2014, ApJ, 789, L25

Cébron D., Vidal J., Schaeffer N., Borderies A., Sauret A., 2021, J. Fluid Mech., 916, A39

Charbonneau P., 2013, Solar and Stellar Dynamos: Saas-Fee Advanced Course 39 Swiss Society for Astrophysics and Astronomy. Springer-Verlag, Berlin, Heidelberg

Charbonneau P., 2014, ARA&A, 52, 251

de Vries N. B., Barker A. J., Hollerbach R., 2023, MNRAS, 524, 2661

Dewberry J. W., 2023, MNRAS, 521, 5991

Dhouib H., Baruteau C., Mathis S., Debras F., Astoul A., Rieutord M., 2024, A&A, 682, A85

Donati J. F., Landstreet J. D., 2009, ARA&A, 47, 333

Dymott R. W., Barker A. J., Jones C. A., Tobias S. M., 2024, MNRAS, 535, 322

Favier B., Barker A. J., Baruteau C., Ogilvie G. I., 2014, MNRAS, 439, 845

Finlay C. C., 2008, in Cardin P., Cugliandolo L.eds, Dynamos. 88 Elsevier Les Houches, p. 403–450,

French M., Becker A., Lorenzen W., Nettelmann N., Bethkenhagen M., Wicht J., Redmer R., 2012, ApJS, 202, 5

Gallet F., Bolmont E., Mathis S., Charbonnel C., Amard L., 2017, A&A, 604, A112

Guseva A., Willis A. P., Hollerbach R., Avila M., 2017, ApJ, 849, 92

Hollerbach R., Rüdiger G., 2005, Phys. Rev. Lett., 95, 124501

Hollerbach R., Teeluck V., Rüdiger G., 2010, Phys. Rev. Lett., 104, 044502

Hori K., Nilsson A., Tobias S. M., 2023, Rev Mod. Plasma Phys., 7, 5

Ji S., Fuller J., Lecoanet D., 2023, MNRAS, 521, 5372

Jones C. A., Boronski P., Brun A. S., Glatzmaier G. A., Gastine T., Miesch M. S., Wicht J., 2011, Icarus, 216, 120

Jouve L., Gastine T., Lignières F., 2015, A&A, 575, A106

Jouve L., Lignières F., Gaurat M., 2020, A&A, 641, A13

Käpylä P. J., Rheinhardt M., Brandenburg A., Käpylä M. J., 2020, A&A, 636, A93

Käpylä P. J., Browning M. K., Brun A. S., Guerrero G., Warnecke J., 2023, Space Sci. Rev., 219, 58

Kirillov O. N., Stefani F., 2010, ApJ, 712, 52

Lander S. K., Jones D. I., Passamonti A., 2010, MNRAS, 405, 318

Lazovik Y. A., Barker A. J., de Vries N. B., Astoul A., 2024, MNRAS, 527, 8245

Le Bars M., Barik A., Burmann F., Lathrop D. P., Noir J., Schaeffer N., Triana S. A., 2022, Surv. Geophys., 43, 229

Lehnert B., 1954, ApJ, 119, 647

Lin Y., 2023, A&A, 671, A37

Lin Y., Ogilvie G. I., 2018, MNRAS, 474, 1644

Malkus W. V. R., 1967, J. Fluid Mech., 28, 793

Mankovich C. R., Fuller J., 2021, Nat. Astron., 5, 1103

Mathis S., 2015, A&A, 580, L3

Mathis S., 2019, in EAS Publ. Ser., France, p.5–33

Meduri D. G., Lignières F., Jouve L., 2019, Phys. Rev. E, 100, 013110

Moffatt H. K., 1978, Magnetic Field Generation in Electrically Conducting Fluids. Cambridge University Press, Cambridge

Morize C., Le Bars M., Le Gal P., Tilgner A., 2010, Phys. Rev. Lett., 104, 214501

Ogilvie G. I., 2009, MNRAS, 396, 794

Ogilvie G. I., 2013, MNRAS, 429, 613

Ogilvie G. I., 2014, ARA&A, 52, 171

Ogilvie G. I., Lin D. N. C., 2004, ApJ, 610, 477

Ogilvie G. I., Lin D. N. C., 2007, ApJ, 661, 1180

Ogilvie G. I., Pringle J. E., 1996, MNRAS, 279, 152

Parker E. N., 1993, ApJ, 408, 707

Petitdemange L., Dormy E., Balbus S., 2013, Phys. Earth Planet. Inter., 223, 21

Pontin C. M., Barker A. J., Hollerbach R., 2024, ApJ, 960, 32

Reese D., Rincon F., Rieutord M., 2004, A&A, 427, 279

Reiners A., 2012, Living Rev. Solar Phys., 9, 1

Rincon F., Rieutord M., 2003, A&A, 398, 663

Rüdiger G., Hollerbach R., Schultz M., Elstner D., 2007, MNRAS, 377, 1481

Schaeffer N., Jault D., Nataf H. C., Fournier A., 2017, Geophys. J. Int., 211, 1

Schmitt D., 2010, Geophys. Astrophys. Fluid Dyn., 104, 135

Schmitt D., Alboussière T., Brito D., Cardin P., Gagnière N., Jault D., Nataf H. C., 2008, J. Fluid Mech., 604, 175

Schmitt D., Cardin P., La Rizza P., Nataf H. C., 2013, Eur. J. Mech. B, 37, 10

Spruit H. C., 1999, A&A, 349, 189

Strugarek A., Beaudoin P., Charbonneau P., Brun A. S., do Nascimento J. D., 2017, Science, 357, 185

Tayler R. J., 1973, MNRAS, 161, 365

Teed R. J., Jones C. A., Tobias S. M., 2014, Geophys. J. Int., 196, 724

Tilgner A., 2007, Phys. Rev. Lett., 99, 194501

Vasil G. M., Lecoanet D., Augustson K., Burns K. J., Oishi J. S., Brown B. P., Brummell N., Julien K., 2024, Nature, 629, 769

Velikhov E. P., 1959, Sov. J. Exp. Theor. Physics, 9, 995

Vidal J., Cébron D., Schaeffer N., Hollerbach R., 2018, MNRAS, 475, 4579

Wahl S. M. et al., 2017, Geophys. Res. Lett., 44, 4649

Wei X., 2016, ApJ, 828, 30

Wei X., 2018, ApJ, 854, 34

Wei X., Goodman J., 2015, ApJ, 806, 50

APPENDIX A: DECAY OF FREE MODES

When injecting the poloidal $\nabla \wedge \nabla \wedge [g(r, \theta, \varphi, t)\boldsymbol{e}_r]$ or the toroidal $\nabla \wedge [h(r, \theta, \varphi, t)\boldsymbol{e}_r]$ magnetic field component into the magnetic diffusion equation $\partial_t \boldsymbol{B} = \mathrm{Em}\,\Delta \boldsymbol{B}$, each potential satisfies a partial differential equation of the form (Moffatt 1978):

$$\frac{\partial f}{\partial t} = \frac{\partial^2 f}{\partial r^2} - \frac{l(l+1)}{r^2}f, \tag{A1}$$

where f stands for either g or h when projecting onto a spherical harmonic of degree l (see also Wei & Goodman 2015). Setting $f = f_l \exp(p_\alpha t)$ with decay rate $-p_\alpha$ and changing variables such that $x^2 = -(p_\alpha/\mathrm{Em})\,r^2$ as in Moffatt (1978, section 2.7), we find that for free decay modes, f_l satisfies Bessel's equation

$$x^2 \frac{\partial^2 f_l}{\partial x^2} + 2x \frac{\partial f_l}{\partial x} + \left[x^2 - l(l+1)\right]f_l = 0, \tag{A2}$$

whose solutions are a linear combination of spherical Bessel functions of the first and second kinds, of fractional order, respectively, $J_{l+1/2}$ and $Y_{l+1/2}$ (Abramowitz & Stegun 1972):

$$f_l = \frac{A}{\sqrt{r}}J_{l+1/2}(k_\alpha r) + \frac{B}{\sqrt{r}}Y_{l+1/2}(k_\alpha r). \tag{A3}$$

Here, A and B are complex constants, and $k_\alpha^2 = -p_\alpha/\mathrm{Em}$. In addition, the poloidal g_l and toroidal h_l potentials are constrained by the insulating boundary conditions at the inner:

$$\partial_r g_l - \frac{l+1}{r}g_l = 0, \text{ and } \partial_r h_l = 0, \quad \text{at} \quad r = \alpha, \tag{A4}$$

and outer spherical surfaces:

$$\partial_r g_l + \frac{l}{r}g_l = 0, \text{ and } \partial_r h_l = 0 \quad \text{at} \quad r = 1. \tag{A5}$$

When combining equations (A3), (A4), and (A5), we can obtain the decay rate $2\,p_\alpha = -2\,\mathrm{Em}\,k_\alpha^2$ of the poloidal or toroidal magnetic energies ($\propto g^2$ or h^2) for a given spherical harmonic degree l at fixed Em. This provides the appropriate application of the derivation of free decay modes in, e.g. Moffatt (1978), to our boundary conditions.

APPENDIX B: INDUCED POLOIDAL MAGNETIC FIELD DURING THE KINEMATIC PHASE

In the simulations for low enough Lehnert numbers, we observe an increase in the poloidal magnetic energy at early times (like in Fig. 2, left panel) possibly due to interactions between non-axisymmetric tidal flows and the toroidal magnetic field. If this interpretation is correct, the generation of a poloidal magnetic field comes from the particular induction term in the induction equation (1b):

$$\nabla \wedge (\boldsymbol{u}_{\mathrm{w}} \wedge \boldsymbol{B}_{\mathrm{t}}) = (\boldsymbol{B}_{\mathrm{t}} \cdot \nabla)\boldsymbol{u}_{\mathrm{w}} - (\boldsymbol{u}_{\mathrm{w}} \cdot \nabla)\boldsymbol{B}_{\mathrm{t}}, \tag{B1}$$

where the non-axisymmetric tidal flow $\boldsymbol{u}_{\mathrm{w}}$ (mostly, the $m = 2$ component) couples with the axisymmetric ($m = 0$) toroidal component of the magnetic field $\boldsymbol{B}_{\mathrm{t}} = \langle B_\varphi \rangle_\varphi \boldsymbol{e}_\varphi$. Indeed, we observe that while the induced toroidal magnetic component is mostly axisymmetric, the axisymmetric component of the poloidal magnetic field just decays with time, so the bump in M_{p} is purely non-axisymmetric (see Fig. 5). Note that the second term on the right-hand side of equation (B1) does not contribute to the energy balance after volume-averaging (only the first term contributes), which makes sense since it locally cancels with part of the first term. Thus, the wave-like poloidal magnetic field in the meridional plane can be written as

$$\boldsymbol{B}_{\mathrm{pw}} = \int_{t_1}^{t_2} \frac{\langle B_\varphi \rangle_\varphi}{s} \left(\boldsymbol{e}_r \partial_\varphi u_r^{\mathrm{w}} + \boldsymbol{e}_\theta \partial_\varphi u_\theta^{\mathrm{w}}\right)\,\mathrm{d}t, \tag{B2}$$

when integrating equation (B1) with time. To compute the non-axisymmetric meridional tidal flow, we set $u_{r,\theta}^{\mathrm{w}} = u_{r,\theta} - \langle u_{r,\theta}\rangle_\varphi$ to remove the background axisymmetric meridional flow. We display the r and θ components of $\boldsymbol{B}_{\mathrm{pw}}$ in Fig. B1 (left panels) choosing $\varphi = 0$. The time integration has been performed between $t_1 = 600$ and $t_2 = 650$ with a time-step of one rotational unit, namely when the poloidal energy is rising and for a short period of time such that Ohmic diffusion does not have time to act. For comparison, the non-axisymmetric components

$$B_{r,\theta}^{\mathrm{noaxi}} = B_{r,\theta}(t_2) - \langle B_{r,\theta}(t_2)\rangle_\varphi - \left[B_{r,\theta}(t_1) - \langle B_{r,\theta}(t_1)\rangle_\varphi\right], \tag{B3}$$

are shown at $\varphi = 0$ between t_2 and t_1 in the right panels. Fig. B1 verifies that our interpretation regarding the leading cause of the generation of poloidal magnetic energy at early times is correct.
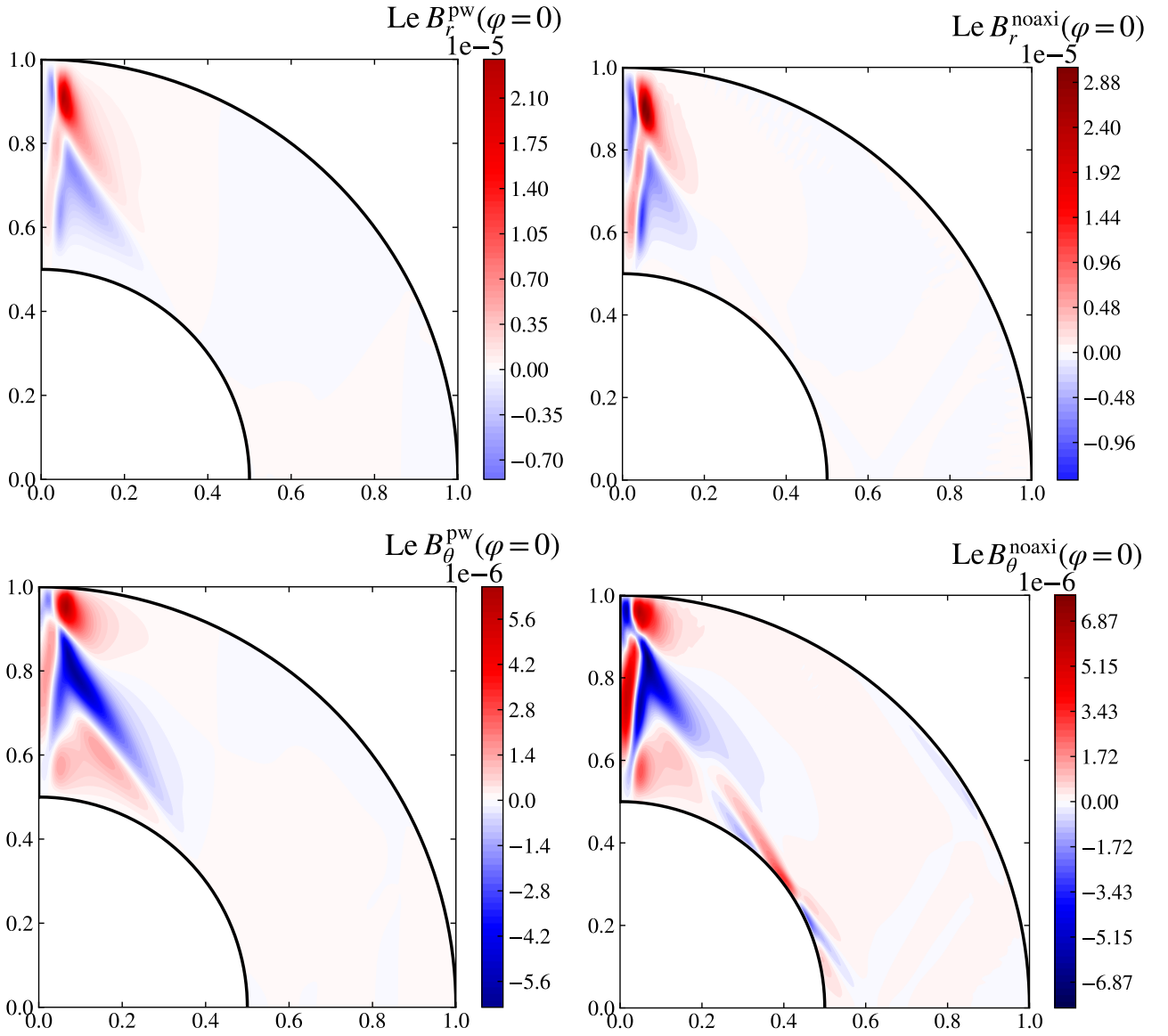
Figure B1. Meridional snapshots in one quadrant at $\varphi = 0$ of the induced wave-like magnetic field equation (B2) (left panels) and the non-axisymmetric magnetic field equation (B3) (right panels) between $t_1 = 600$ and $t_2 = 650$ from a simulation with $\mathrm{Le} = 10^{-5}$ and $\mathrm{Pm} = 1$. For each row, the intensity of the colour scales with the same extrema (which are symmetric). Top: r-components. Bottom: θ-components.
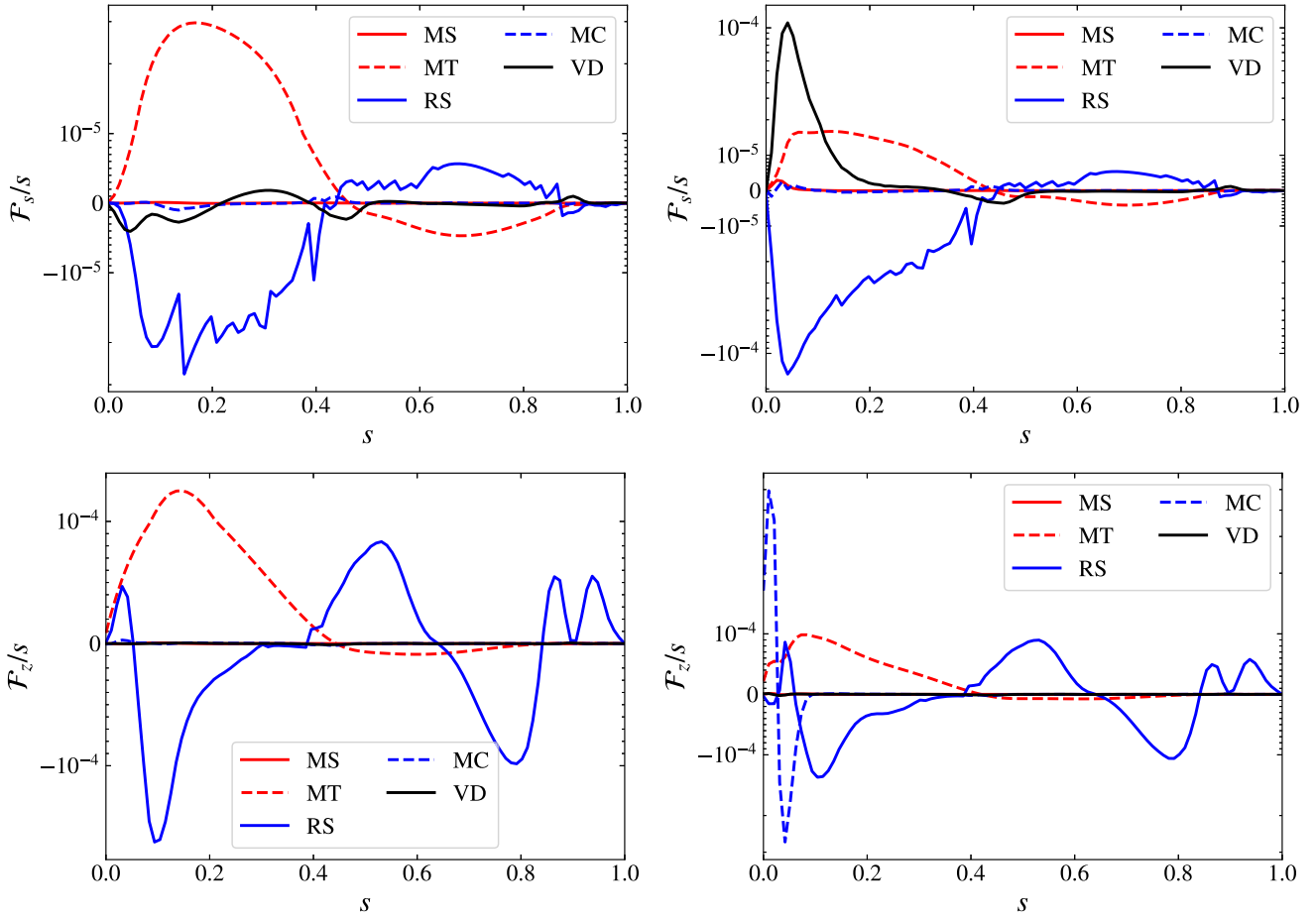
Figure B2. Flux terms within the cylindrical $\mathcal{F}_s/s$ (top) and vertical $\mathcal{F}_z/s$ (bottom) angular momentum fluxes, integrated along z over the North hemisphere only, for Le $= 10^{-2}$ and Pm $= 1$. Left: $t \approx 6500$ close to a local minimum for the zonal flow amplitude. Right: $t \approx 7150$ close to a local maximum for the zonal flow amplitude.
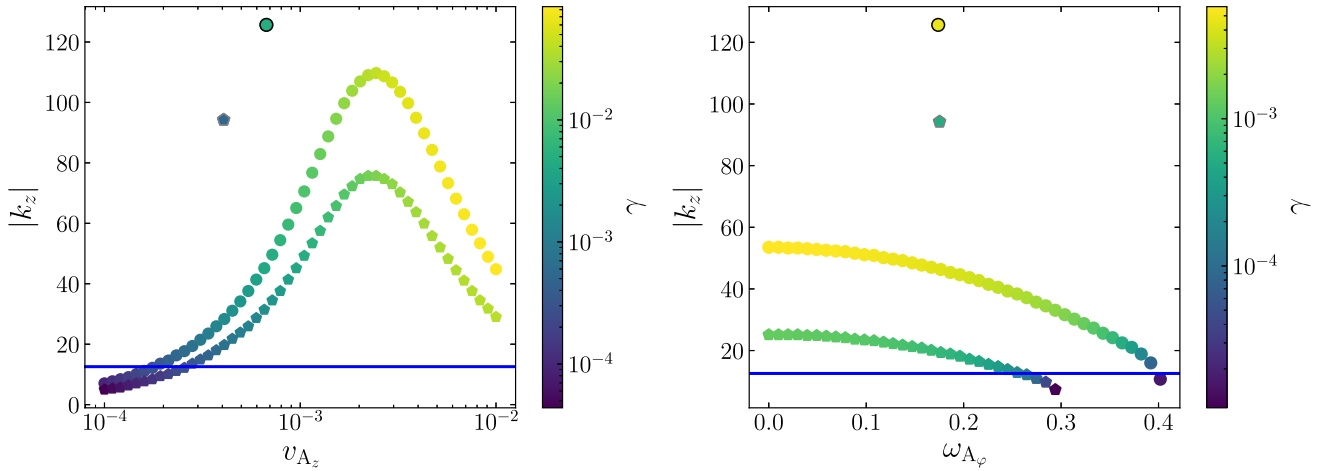
Figure B3. Fastest growing modes with growth rates γ and vertical wavenumbers k_z from SMRI/HMRI local stability analysis with axisymmetric vertical and azimuthal magnetic fields whose strengths are given by v_{A_z} (left) and ω_{A_φ} (right). Bullets and pentagons correspond, respectively, to predictions for Le $= 4 \times 10^{-4}$ and 10^{-3} using the specific sets of parameters $(S_\Omega, \Omega, \omega_{A_\varphi})$ (left panel) and $(S_\Omega, \Omega, v_{A_z})$ (right) given in Table C1 for the two simulations. Black/grey outlined symbols correspond to the associated estimations using the values in Table C1 and the axisymmetric growth rates in Table 3. The lower limit $k_z = 2\pi/(1 - \alpha)$ is indicated by a blue line.

APPENDIX C: LOCAL LINEAR STABILITY ANALYSES

C1 Axisymmetric (helical and standard) magnetorotational instabilities

We adopt the approach of Kirillov & Stefani ([2010](#)) to analyse the growth of axisymmetric perturbations in a differentially rotating incompressible fluid in the presence of both a poloidal and toroidal magnetic field. This employs a local WKBJ approximation around a fiducial point (s, z). Linearized axisymmetric ($m = 0$) perturbations can be sought for each variable proportional to $\exp(\gamma t + ik_s s + ik_z z)$, where γ is the complex growth rate (at least when $\mathrm{Re}[\gamma] > 0$), and k_s and k_z are the cylindrical radial and vertical wavenumbers, respectively (assumed to be real). The unstable modes can be determined by solving the resulting dispersion relation, which is the following degree 4 polynomial (see Kirillov & Stefani [2010](#), for details of the derivation):

$$\gamma^4 + a_1\gamma^3 + a_2\gamma^2 + (a_3 + ib_3)\gamma + a_4 + ib_4 = 0, \tag{C1}$$

where the coefficients are:

$$a_1 = 2(\omega_\nu + \omega_\eta),$$
$$a_2 = (\omega_\nu + \omega_\eta)^2 + 2(\omega_A^2 + \omega_\nu\omega_\eta) + \alpha^2\kappa^2 + 4\alpha^2\omega_{A_\varphi}^2,$$
$$a_3 = 2(\omega_\eta + \omega_\nu)(\omega_A^2 + \omega_\nu\omega_\eta) + 2\alpha^2\kappa^2\omega_\eta + 4\alpha^2(\omega_\eta + \omega_\nu)\omega_{A_\varphi}^2,$$
$$a_4 = (\omega_A^2 + \omega_\nu\omega_\eta)^2 - 4\alpha^2\omega_A^2\Omega^2 + \alpha^2\kappa^2(\omega_A^2 + \omega_\eta^2) + 4\alpha^2\omega_\nu\omega_\eta\omega_{A_\varphi}^2,$$
$$b_3 = -8\alpha^2\Omega\omega_A\omega_{A_\varphi},$$
$$b_4 = -4\alpha^2\Omega\omega_A\omega_{A_\varphi}(2\omega_\eta + \omega_\nu) - \kappa^2\alpha^2\Omega^{-1}\omega_A\omega_{A_\varphi}(\omega_\eta - \omega_\nu). \tag{C2}$$

We have also defined

$$k = \sqrt{k_z^2 + k_s^2}, \quad \alpha = \frac{k_z}{k}, \quad \Omega = \Omega_0 + \delta\Omega(s)$$
$$\omega_A = \frac{k_z B_z}{\sqrt{\mu_0\rho}}, \quad \omega_{A_\varphi} = \frac{B_\varphi}{\sqrt{\mu_0\rho}\,s},$$
$$\omega_\nu = \nu k^2, \quad \omega_\eta = \eta k^2, \quad \kappa^2 = 2\Omega\left(2\Omega + \frac{d\,\delta\Omega}{d\ln s}\right) = 2\Omega(2\Omega - S_\Omega). \tag{C3}$$

This dispersion relation for axisymmetric modes describes the SMRI acting on a purely poloidal field if $B_\varphi = 0$ (e.g. Balbus & Hawley [1991](#), [1998](#)) and the HMRI involving a combination of a poloidal and toroidal field otherwise (e.g. Hollerbach & Rüdiger [2005](#); Kirillov & Stefani [2010](#)). The presence of toroidal magnetic fields can affect some axisymmetric modes through hoop stresses, which is why B_φ appears in the dispersion relation, unlike in analyses that adopt a purely local Cartesian model (e.g. Dymott et al. [2024](#)).

Since it is not straightforward to choose a specific fiducial point (s, z) where to apply the local stability analysis to our simulations (especially in the vertical direction), we arbitrarily choose to take $s = s_m$ where the φ- and z-averaged shear parameter $S_\Omega = -d\delta\Omega/d\ln s$ is maximized at a specific time t. We then take the φ and z average of the azimuthal Alfvén frequency ω_{A_φ}, the vertical Alfvén velocity $v_{A_z} = \omega_A/k_z$ (defined to get rid of k_z in ω_A), and the rotation rate Ω, at this location s_m. The values of these parameters are displayed in Table [C1](#) for the two simulations showing signs of MHD instabilities at a time where M_p is maximized (second peak for Le $= 10^{-3}$ shown in Fig. [16](#)). The vertical wavenumber $k_z = 2\pi/\lambda_z$ is estimated by computing the number of vertical wavelengths λ_z in the domain in Fig. [15](#) (left panels). Lastly, the viscous and Ohmic decay rates ω_ν and ω_η are computed using the global (mag-

netic) Ekman number Ek $= 10^{-5}$ and Em $=$ Ek/Pm $= 2 \times 10^{-6}$ for Pm $= 5$.

In Fig. [B3](#), we present predictions for growth rates γ and vertical wavenumbers k_z from solving equation ([C1](#)) with the parameters given in equations ([C2](#)) and ([C3](#)). We do so by varying either ω_{A_φ} or v_{A_z}, and fixing the other parameters to the values listed in Table [C1](#). Only the fastest growing mode is selected for each set of parameters, which is always found to have $k_s = 0$ ('channel modes'). Increasing the strength of the azimuthal magnetic field (by increasing ω_{A_φ}) reduces both γ and k_z compared to SMRI with $B_\varphi = 0$. Conversely, increasing v_{A_z} boosts the growth rate, but not necessarily the value of k_z, which decays after a maximum around $v_{A_z} \approx 2.3 \times 10^{-3}$. This may be related to some known properties for SMRI. Without diffusion, this would predict $\lambda_z \propto B_z$, so $k_z \propto 1/B_z \propto 1/v_{A_z}$. With diffusion, this would be modified for small B_z where those smaller scale modes would be damped. Also, B_φ would presumably play a role also in causing this maximum. Monotonic growth of both the maximum γ and the corresponding k_z is observed with increases in the shear parameter S_Ω (not shown here). The modes predicted below the threshold $k_z = 2\pi/(1 - \alpha)$ (blue line) should not be able to develop in the shell (with size $1 - \alpha$), since they would be larger than the domain size. Values of the growth rate measured in the simulations (from $M_p(m = 0)$ in Table [3](#)) are indicated in grey/black outlined symbols in both panels of Fig. [B3](#) using the values of k_z, ω_{A_φ}, and v_{A_z} listed in Table [C1](#). The measured growth rates match quite well the analytically predicted ones, which are around 4×10^{-3} and 7×10^{-4} for Le $= 4 \times 10^{-4}$ and 10^{-3}, respectively. However, the predicted vertical wavenumbers are lower than the estimates in Table [C1](#). If the most unstable mode is not taken, but k_z is instead fixed to the last column of Table [C1](#), the predicted modes would be stable. However, it must be stressed that the values for S_Ω, ω_{A_φ}, Ω, and v_{A_z} vary substantially from one fiducial point to another (and the z-average reduces values of S_Ω and v_{A_z}, and thus of k_z), while the growth rate has been measured from a global poloidal quantity, which does not make the comparison with the local analytical model straightforward. Moreover, the validity of this local dispersion relation relies on several assumptions that may not be fully satisfied in our global simulations. First, the cylindrical and vertical variations are assumed to be small compared with the characteristic length-scales of variation of background flow and field quantities in the same directions. This is probably justified in the vertical direction, where the zonal flow and the vertical and azimuthal magnetic fields are mainly invariant of z. However, it is marginally satisfied in the radial direction, since the variation along s in Fig. [15](#) is only slightly smaller than the typical length-scale on which the shear varies $l_\Omega \sim 0.1$. In addition, the short-wavelength approximation relies on the fact that $k_s s \gg 1$, which is not satisfied here. Nevertheless, these results are suggestive that the MRI is in operation in our simulations.

C2 Non-axisymmetric azimuthal magnetic instabilities

In this section, we apply the local analytical model derived in Meduri et al. ([2019](#)) to investigate AMRI involving the growth of non-axisymmetric perturbations in an incompressible and differentially rotating fluid with a dominant azimuthal magnetic field (first derived by Acheson & Gibbons [1978](#), but here we omit buoyancy and thermal diffusion). The overall approach is similar to that in Appendix [C1](#) to derive a dispersion relation, but here we consider the presence of only an axisymmetric azimuthal magnetic field. By injecting non-axisymmetric small-amplitude perturbations of the form $\exp\{i(k_s s + k_z z + m\varphi - \sigma t)\}$ into the governing equations and
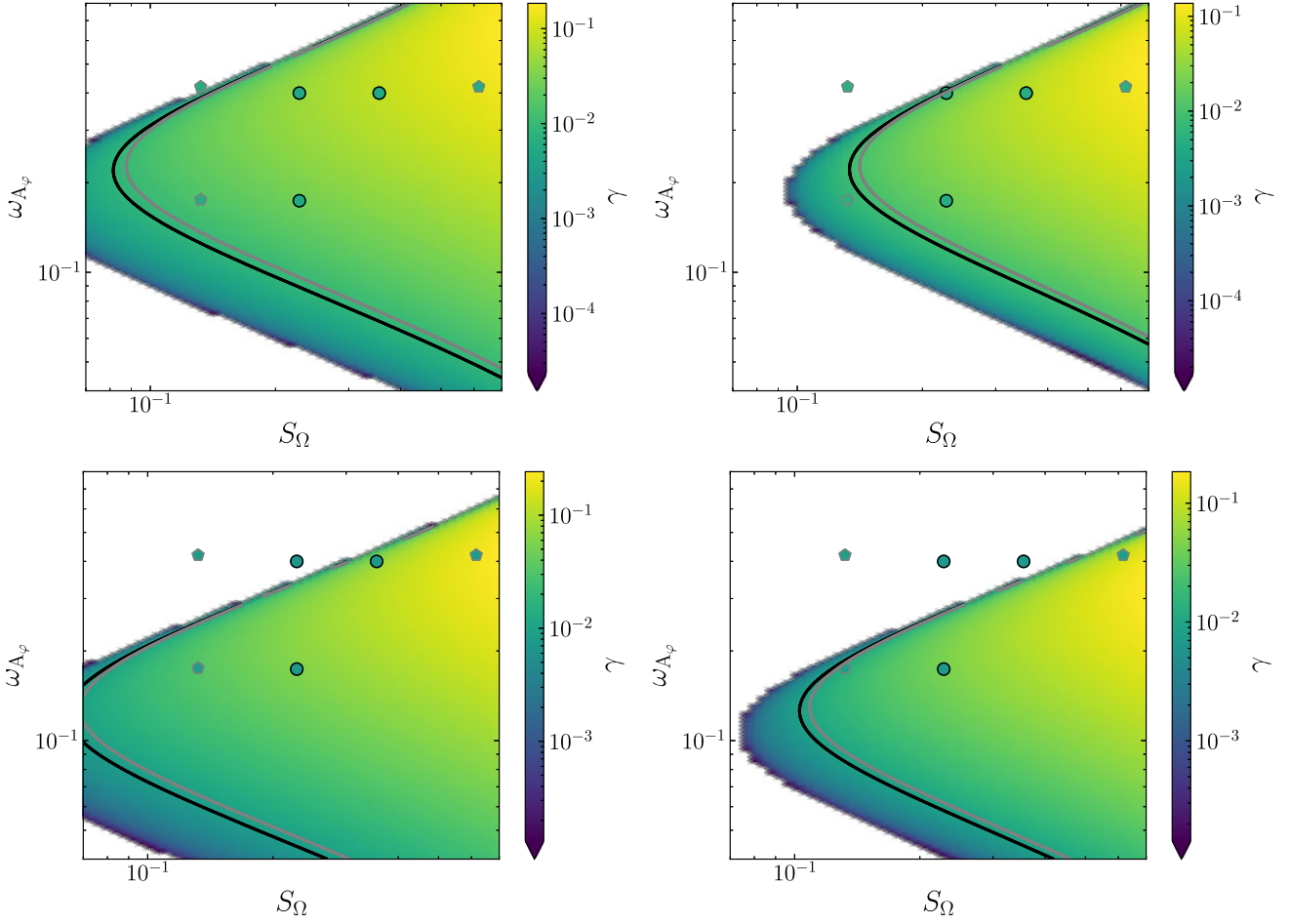
Figure C1. Predictions for the growth rate γ due to non-axisymmetric AMRI for a fixed vertical wavenumber $k_z = 94$ as a function of the shear parameter S_Ω and the azimuthal Alfvén frequency ω_{A_φ}. As in Fig. B3, black outlined bullets are for Le $= 4 \times 10^{-4}$ and grey pentagons are for Le $= 10^{-3}$. These refer to growth rate estimates using either z-averaged $(S_\Omega, \omega_{A_\varphi})$ from Table C1 (lowest pair of symbols), the maximum of $(S_\Omega, \omega_{A_\varphi})$ over z at $s_{\rm m}$ (upper right pair symbols), or a mix of the two (upper left pair of symbols), and the highest non-axisymmetric growth rates of the toroidal magnetic energy in Table 3. Associated contour lines are also indicated in black (for $\gamma = 8 \times 10^{-3}$) and grey (for $\gamma = 10^{-2}$). The white region indicates stable modes (with zero growth). Left: $k_x = 0$. Right: $k_x = 63$. Up: $m = 1$. Down: $m = 2$.

Table C1. Values chosen to apply the HMRI and AMRI local stability analyses. The φ and z averaged parameters v_{A_z}, ω_{A_φ}, Ω, and S_Ω have been evaluated at a fiducial point $s_{\rm m}$ which maximizes $\langle S_\Omega \rangle_z$ in the upper hemisphere at a time t. The vertical wavenumber k_z is measured from the left panels of Fig. 15.

Le	t	$s_{\rm m}$	v_{A_z}	ω_{A_φ}	Ω	S_Ω	k_z
4×10^{-4}	4850	0.044	6.7×10^{-4}	0.17	1.2	0.23	126
10^{-3}	2950	0.044	4.1×10^{-4}	0.18	1.1	0.13	94

linearizing (around the background axisymmetric state), we can obtain the dispersion relation below. The growth rate is $\gamma = \Im\sigma$ when the fluid is unstable ($\Im\sigma > 0$) and the vertical and (cylindrical) radial wavenumbers are again k_z and k_s. The azimuthal wavenumber m is fixed to 1 or 2 in the following analysis, motivated by our simulations. In this framework, the dispersion relation is again a fourth-order polynomial:

$$a_4 \tilde\omega^4 + a_3 \tilde\omega^3 + a_2 \tilde\omega^2 + a_1 \tilde\omega + a_0 = 0, \qquad (C4)$$

with $\tilde\omega = \sigma/\Omega - m$ the dimensionless Doppler-shifted frequency, and with coefficients:

$$a_4 = 1 + \beta^2,$$
$$a_3 = 2i\left(1 + \beta^2\right)\left(\text{Re}^{-1} + \text{Rm}^{-1}\right),$$
$$a_2 = -2(q+2) + 2\text{L}_\text{o}^2\left[b - 1 - m^2\left(1 + \beta^2\right)\right]$$
$$\quad - \left(1 + \beta^2\right)\left(\text{Re}^{-2} + \text{Rm}^{-2} - 4\text{Re}^{-1}\text{Rm}^{-1}\right),$$
$$a_1 = -8m\text{L}_\text{o}^2 + i\left\{2\text{L}_\text{o}^2\left[b - 1 - \left(1 + \beta^2\right)m^2\right]\left(\text{Re}^{-1} + \text{Rm}^{-1}\right)\right.$$
$$\quad\left. - 4(2+q)\text{Rm}^{-1} - 2\left(1 + \beta^2\right)\left(\text{Re}^{-2}\text{Rm}^{-1} + \text{Re}^{-1}\text{Rm}^{-2}\right)\right\},$$
$$a_0 = m^2\text{L}_\text{o}^2\left\{2q - \text{L}_\text{o}^2\left[2(b+1) - \left(1 + \beta^2\right)m^2\right]\right\}$$
$$\quad - 2\text{L}_\text{o}^2\left[b - 1 - \left(1 + \beta^2\right)m^2\right]\text{Re}^{-1}\text{Rm}^{-1} + \left(1 + \beta^2\right)\text{Re}^{-2}\text{Rm}^{-2}$$
$$\quad + 2(2+q)\text{Rm}^{-2} + i\left\{2m\text{L}_\text{o}^2\left[q\text{Re}^{-1} - (4+q)\text{Rm}^{-1}\right]\right\}. \qquad (C5)$$

In equation (C5), six additional dimensionless parameters have been introduced (along with $k = \sqrt{k_s^2 + k_z^2}$):

$$\beta = \frac{k_s}{k_z}, \quad \text{Re} = \frac{\Omega}{\nu k^2}, \quad \text{Rm} = \frac{\Omega}{\eta k^2}, \quad q = \frac{\partial \ln \Omega}{\partial \ln s} - \beta \frac{s}{z} \frac{\partial \ln \Omega}{\partial \ln z},$$
$$\text{L}_\text{o} = \frac{\omega_{A_\varphi}}{\Omega} = \frac{B_\varphi}{\sqrt{\mu\rho}s\Omega}, \quad b = \frac{1}{2}\left(\frac{\partial \ln B_\varphi^2}{\partial \ln s} - \beta \frac{s}{z} \frac{\partial \ln B_\varphi^2}{\partial \ln z}\right), \qquad (C6)$$

quantifying, in order, the poloidal wavenumber ratio, the hydrodynamical and magnetic Reynolds numbers, the shear rate, and the azimuthal magnetic field amplitude and its gradient. This dispersion relation describes non-axisymmetric magnetorotational (differential rotation-driven) instabilities and the Tayler (current-driven) instability (Tayler [1973](#); Ji, Fuller & Lecoanet [2023](#), for instance in MHD simulations).

In our simulations, the zonal flow depends mainly on s, such that $\Omega = 1 + \delta\Omega(s)$, so its vertical gradient can be neglected and the shear parameter can be approximated by $q \approx \partial \ln \Omega / \partial \ln s \approx -S_\Omega / \Omega$. The vertical gradient in b is also quite weak in the region where instability is observed, with $(s/z)\,\partial \ln B_\varphi^2 / \partial \ln z \lesssim 10^{-3}$, and the radial gradient is of the order of unity with $\partial \ln B_\varphi^2 / \partial \ln s \approx 1$. We choose the same fiducial point $s_{\rm m}$ as for SMRI/HMRI in Table [C1](#), as well as the same values for ω_{A_φ}, Ω, and S_Ω. To illustrate the variability of the parameters in the simulations, the growth rate computed using the maximum (along z) shear rate and azimuthal Alfvén frequency are also displayed when computing the estimates (symbols in Fig. [C1](#)). The Reynolds numbers Re and Rm are computed using the global (magnetic) Ekman number ${\rm Ek} = 10^{-5}$ and ${\rm Em} = {\rm Ek}/{\rm Pm} = 2 \times 10^{-6}$ together with the appropriate value of k.

Contrary to our axisymmetric SMRI/HMRI stability analysis, we choose to fix the wavenumbers.[15] Here, k_z and k_s are fixed and we vary ω_{A_φ} and S_Ω, as is shown in Fig. [C1](#), setting the local rotation rate to the maximum of the two simulations $\Omega = 1.2$. The vertical wavenumber has been set to $k_z = 94$ as estimated for ${\rm Le} = 4 \times 10^{-4}$, and $k_s = 63$ in the right panel is a rough estimation of the radial wavenumber $k_s = 2\pi/\lambda_s$ in Fig. [15](#), with λ_s the cylindrical radial wavelength. We pick $m = 1$, since it is expected to be the azimuthal wavenumber of the most unstable non-axisymmetric mode (see e.g. Hollerbach et al. [2010](#), and Fourier transform of the toroidal velocity reveals that this component is non-negligible after the instability is triggered for ${\rm Le} = 4 \times 10^{-4}$ and 10^{-3}), along with the $m = 2$ forced mode in our simulations. The main effect of increasing k_z (not shown here) is to reduce the extent of the unstable region for small ω_{A_φ} and small S_Ω. Increasing k_s has the same effect, and more specifically shifts the region of unstable modes to higher shear rates S_Ω, as seen when comparing the two columns of Fig. [C1](#). Higher azimuthal wavenumbers shift the region of unstable modes to lower azimuthal Alfvén frequencies for which the restoring effects of magnetic tension are weaker. Unlike for SMRI/HMRI, an increase of the azimuthal Alfvén frequency implies a larger growth rate. Larger growth rates are also found for higher shear S_Ω. The term encoding radial and vertical gradient of the azimuthal magnetic field in equation ([C5](#)) may not play an important in our model, since

putting $b = 0$ instead does not alter much the growth rate, which probably rules out the possibility of a Tayler-type instability.

Depending on the value used for the shear (either $\max\langle S_\Omega \rangle_z$ or $\max[S(s_{\rm m}, z)]$) and for the azimuthal Alfvén wave frequency (either $\langle \omega_{A_\varphi}(s_m) \rangle_z$ or $\max[\omega_{A_\varphi}(s_{\rm m}, z)]$), analytical predictions for the growth rate can be found quite close to the measured values for both $m = 1$ and 2, though higher growth rates (when values are in the unstable region) are often predicted theoretically. Hence, non-axisymmetric MRI is a plausible explanation for the instability observed in these simulations, potentially in addition to axisymmetric MRI.

We caution once again regarding the difficulty of choosing the fiducial point, which has a major impact on the parameter values and the uncertainty surrounding our predictions of the growth rates and wavenumbers. Moreover, the short-wavelength approximation assumes the meridional wavelength perturbation

$$\lambda_{\rm m} = \sqrt{\lambda_s^2 + \lambda_z^2} \ll r, l_{B_\varphi}, l_\Omega, \tag{C7}$$

with r the spherical radius, $l_{B_\varphi} = |\nabla \ln B_\varphi|^{-1}$ and $l_\Omega = |\nabla \ln \Omega|^{-1}$ the scale heights of the azimuthal magnetic field and rotation. Since vertical variations of B_φ and Ω are negligible compared to radial variations, the scale heights can be written as $l_{B_\varphi} \approx 2s/|\partial \ln B_\varphi^2 / \partial \ln s|$ and $l_\Omega \approx |\partial_s \ln \Omega|^{-1}$, both taking values of order 0.1, like r. Depending on the value of λ_s, the condition equation ([C7](#)) is either not satisfied (if $k_s = 63$, $\lambda_{\rm m} \sim 0.1 \sim r, l_{B_\varphi}, l_\Omega$) or is only marginally satisfied (if $k_s = 0$, $\lambda_{\rm m} \sim 5 \times 10^{-2} \lesssim r, l_{B_\varphi}, l_\Omega$). Moreover, the azimuthal wavelength of the perturbations must also satisfy $\lambda_{\rm m} \ll \lambda_\varphi$, which is not well verified with $\lambda_\varphi = 2\pi s_{\rm m}/m \sim 10^{-1} \sim \lambda_{\rm m}$ if $m = 1$ and 2. Finally, and perhaps most importantly, we also require the growth time for the instability to be (much) shorter than the time-scale to shear out non-axisymmetric perturbations for a (exponentially growing in time) normal-mode analysis to be valid. This requires

$$m \ll k_s \frac{l_\Omega}{\Omega} \gamma_{\max}, \tag{C8}$$

with $\gamma_{\max}$ the maximum growth rate of the most unstable mode for a specific set of parameters $(\omega_{A_\varphi}, S_\Omega)$ (see equation 26 of Meduri et al. [2019](#), and the associated arguments). The right-hand side of equation ([C8](#)) is evaluated here to be, at most, $63 \times 0.1 \times 10^{-1} \lesssim 1 \lesssim m$, implying that non-axisymmetric perturbations with $m = 1$ and 2 will be substantially modified by the shear over the predictions of this normal-mode theory. In this case, a transient amplification of non-axisymmetric modes is predicted instead, and the consequent increase in k_s with time due to the action of the shear will enhance the effects of diffusion and ultimately stabilize the modes. In addition, the larger magnetic tension acting on these larger k_s modes may also help to stabilize them. Hence, we expect the observed growth rates to be smaller than the theoretical predictions, just as we have observed numerically.

---

[15] We adopt this approach, as in Meduri et al. ([2019](#)), because the fastest growing mode typically has very small $k_s, k_z \ll 1$.

This paper has been typeset from a TeX/LaTeX file prepared by the author.